Amidase and Lysozyme Dual Functions in TseP Reveal a New Family of Chimeric Effectors in the Type VI Secretion System

Running title: Chimeric effector with dual functions

Zeng-Hang Wang[1,2], Ying An[2], Ting Zhao[3,4], Tong-Tong Pei[2], Dora Yuping Wang[2,5], Xiaoye Liang[2], Wenming Qin[3*], Tao Dong [2*]

Affiliations:

[1] State Key Laboratory of Microbial Metabolism, Joint International Research Laboratory of Metabolic & Developmental Sciences, School of Life Sciences and Biotechnology, Shanghai Jiao Tong University, Shanghai, 200240, China

[2] Department of Immunology and Microbiology, School of Life Sciences, Southern University of Science and Technology, 518055, Shenzhen, China

[3] National Facility for Protein Science in Shanghai, Shanghai Advanced Research Institute, Chinese Academy of Sciences, Shanghai, 201210, People's Republic of China

[4] School of Pharmaceutical Sciences, Wuhan University, Wuhan, China

[5] Department of Physiology, University of Toronto, Toronto, Canada

[*] Correspondence to dongt@sustech.edu.cn；qinwenming@sari.ac.cn

Keywords: protein secretion, effector, peptidoglycan, amidase, synthetic biology

Abstract

Peptidoglycan (PG) serves as an essential target for antimicrobial development. An overlooked reservoir of antimicrobials lies in the form of PG-hydrolyzing enzymes naturally produced for polymicrobial competition, particularly those associated with the type VI secretion system (T6SS). Here we report that a T6SS effector TseP, from *Aeromonas dhakensis*, represents a family of effectors with dual amidase-lysozyme activities. *In vitro* PG-digestion coupled with LC-MS analysis revealed the N-domain's amidase activity, which is neutralized by either catalytic mutations or the presence of the immunity protein TsiP. The N-domain, but not the C-domain, of TseP is sufficient to restore T6SS secretion in T6SS-defective mutants, underscoring its critical structural role. Using pull-down and secretion assays, we showed that these two domains interact directly with a carrier protein VgrG2 and can be secreted separately. Homologs in *Aeromonas hydrophila* and *Pseudomonas syringae* exhibited analogous dual functions. Additionally, N- and C-domains display distinctive GC contents, suggesting an evolutionary fusion event. By altering the surface charge through structural-guided design, we engineered the $TseP^{C4+}$ effector that successfully lyses otherwise resistant *Bacillus subtilis* cells, enabling the T6SS to inhibit *B. subtilis* in a contact-independent manner. This research uncovers TseP as a new family of bifunctional chimeric effectors targeting PG, offering a potential strategy to harness these proteins in the fight against antimicrobial resistance.

Significance Statement

Antimicrobial resistance urgently demands global interventions, and the bacteria cell wall remains a promising target. Our research introduces a novel family of bifunctional, cell-wall-damaging T6SS effectors. More importantly, we demonstrate an effective strategy to enable an otherwise ineffective enzyme to target both Gram-negative and Gram-positive bacteria. Our findings highlight a promising path forward using cell-wall-damaging effectors, a largely untapped resource, in the fight against antimicrobial resistance.

26 **Introduction**

27 Antimicrobial resistance (AMR) is a critical global health crisis, with bacterial AMR implicated
28 in approximately 4.95 million deaths in 2019, and predictions estimating up to 10 million deaths per year
29 by 2050 (1, 2). Developing novel antimicrobials is thus of paramount importance but also a highly
30 challenging task. Bacterial cell walls, mainly composed of peptidoglycan (PG) and crucial for survival,
31 serve as a primary target for antimicrobials. However, the discovery of conventional PG-inhibiting small
32 molecules is impeded by fewer choices and increasing resistance (3, 4). The naturally occurring PG-
33 lysing enzymes, secreted by bacteria for competition in polymicrobial environments (5–8), remain
34 underexplored for AMR treatment.

35 As a widespread molecular weapon in Gram-negative bacteria, the type VI secretion system
36 (T6SS) can directly inject PG-lysing enzymes and other antibacterial toxins into neighboring microbes
37 and anti-eukaryotic toxins to yeast and mammalian cells(7, 9–15). The conserved structure of T6SS
38 consists of a double tubular structure, a baseplate TssEFGK complex, and a transmembrane TssJLM
39 complex (16–19). A spear-like inner tube, made of stacks of Hcp hexamers, is ejected outward upon
40 contraction of an outer sheath made of stacks of TssB/C hexamers, and a VgrG-PAAR spike complex
41 sitting atop the Hcp tube is delivered concomitantly (12, 20, 21). Although the ejected Hcp spear can
42 penetrate neighboring bacterial cells, T6SS-elicited damages are largely dependent on the secreted
43 effectors rather than the penetration (22–24). Numerous T6SS effectors have been predicted in Gram-
44 negative bacteria, and known effectors display diverse functions including damaging the cell wall and
45 membrane, DNase, and metal scavenging (6, 25–30). Despite the functional diversity of T6SS effectors,
46 PG-targeting effectors seem to be most commonly associated with the T6SSs.

47 The conserved structure of PG comprises repeating disaccharide units of N-acetylglucosamine
48 (NAG) and N-acetylmuramic acid (NAM), with a short peptide (most commonly $_{L}$-Ala-$_{D}$-Glu-*m*-DAP-
49 $_{D}$-Ala-$_{D}$-Ala) attached to each NAM (31). Adjacent peptide chains of PG are cross-linked, forming a
50 continuous network that envelops bacterial cells (31). T6SS effectors known to target PG fall into two

51 categories, T6SS amidase/endopeptidase (Tae) families cleaving the peptides and T6SS glycoside
52 hydrolase (Tge) families cleaving the glycan backbone. Tae effectors have been found to cleave bonds
53 between $_{D}$-Glu and *m*DAP, between *m*DAP and $_{D}$-Ala, and between NAM and $_{L}$-Ala (7, 27, 32, 33). Tge
54 effectors possess β-(1-4)-N-acetyl-muramidase activities and N-acetylglucosaminidase activities (5, 6,
55 27, 34). The recent discovery of Tse4 in *Acinetobacter baumannii*, cleaving both the glycan strand and
56 the crosslinked peptide cross-bridge, suggests dual enzymatic activities could be found in a single
57 effector (10). However, such bifunctionality among effectors is rare.

58 As a ubiquitous waterborne pathogen, *Aeromonas dhakensis* can cause soft tissue infection and
59 bacteremia in fish and humans (35, 36). The T6SS of *A. dhakensis* type strain SSU is active under
60 laboratory conditions and can secrete three known antimicrobial effectors, a membrane-targeting TseC,
61 a lysozyme-like TseP, and a nuclease TseI (25, 37–40). Our previous findings have established that TseP
62 serves a structural role because its expression can restore the T6SS secretion in the Δ*3eff* mutant lacking
63 all three effector genes, and the C-terminal domain, $TseP^{C}$, possesses lysozyme activities (38). However,
64 the function of the N-terminal domain, $TseP^{N}$, which lacks any recognizable conserved motif, has
65 remained elusive. This study unveils $TseP^{N}$ is capable of cleaving the peptide link between NAM and $_{L}$-
66 Ala as an amidase. Both $TseP^{N}$ and $TseP^{C}$ can be secreted separately by the T6SS, but only $TseP^{N}$ can
67 compensate for T6SS defects, indicating its critical role as a structural component. Additionally, $TseP^{N}$
68 exhibits approximately 10% higher GC content than $TseP^{C}$, and homologs of $TseP^{N}$ and $TseP^{C}$ exist
69 independently in divergent species. This disparity in GC content and the presence of domain-specific
70 homologs suggest an evolutionary fusion event. We further show that $TseP^{C}$ can be engineered to
71 hydrolyze resistant Gram-positive *Bacillus subtilis* cells, conferring the T6SS with the capability to kill
72 Gram-positive bacteria in a contact-independent manner. This research identifies a novel class of
73 amidase-lysozyme bifunctional effectors, provides insights into effector evolution, and highlights the
74 potential of engineering these effectors as antimicrobials.

75

76 **Results**

77 **TseP^N and TseP^C can be independently secreted by the T6SS**

78 To delineate the regions of TseP crucial for T6SS-mediated secretion, we constructed two TseP
79 truncations, TseP^N and TseP^C, and then expressed them in the Δ*3eff* mutant using the pBAD arabinose-
80 inducible vectors. Consistent with our previous results, protein secretion assays show that the Δ*3eff*
81 mutant, akin to the T6SS null Δ*vasK*, failed to secrete Hcp (Figure 1A). Complementation with TseP and
82 TseP^N, but not TseP^C, restored Hcp secretion, despite at a reduced level relative to the wild type (Figure
83 1A). We next tested whether the T6SS assembly is restored using a chromosomal sheath-labeled
84 construct TssB-sfGFP. Fluorescence microscopy analysis showed that complementation with both TseP
85 and TseP^N, but not the TseP^C, restored sheath assembly (Figure 1, B and C). Because both Hcp secretion
86 and sheath assembly are hallmarks of T6SS assembly, these findings highlight the important structural
87 role of the TseP N-terminus.

88 Interestingly, we noticed that TseP^N, but not TseP^C, was secreted (Figure 1A). The lack of TseP^C
89 secretion might be due to a defective T6SS. To test this, we expressed different plasmid-borne TseP
90 constructs in a panel of SSU mutant strains. Western blot analysis not only confirmed the secretion of
91 TseP and TseP^N but also detected the secretion of TseP^C, albeit to a lesser extent, in both wild-type and
92 the Δ*tseP* cells (Figure 1D). Considering that VgrG2 is the carrier protein for TseP delivery (38), we next
93 tested whether TseP^N and TseP^C could interact with VgrG2. Pull-down analysis showed direct interaction
94 of VgrG2 with TseP^N and TseP^C, in contrast to the sfGFP and MBP negative controls (Figure 1E). These
95 results indicate TseP^N and TseP^C can be secreted independently by the T6SS.

96 **TseP^N is a Zn^{2+}-dependent amidase**

97 When analyzing TseP-mediated PG hydrolysis products using ultraperformance liquid
98 chromatography coupled with mass spectrometry (UPLC-MS), we detected two distinctive peaks and
99 determined their corresponding products to be NAM-NAG disaccharides and Tri/Tetra peptides (Figure
100 2, A and B), the latter suggesting an amidase activity. The released peptides were also detected in samples

101 treated with $TseP^N$ and the catalytically inactive C-terminal lysozyme mutant $TseP^{E663A}$, but not with
102 $TseP^C$ or its inactive $TseP^{C\text{-}E663A}$ mutant, indicating that the amidase activity is attributed to $TseP^N$.

103 Sequence comparison with known amidases suggests that the $TseP^N$ contains a predicted Zn^{2+}
104 binding domain with several conserved residues H19, H23, H109, H339, H359, and E539 (Figure 2C).
105 To test the effect of these residues on the $TseP^N$ amidase, we replaced these sites with alanines using site-
106 directed mutagenesis and then purified a set of $TseP^N$ mutant proteins. Subsequent PG-digestion assays,
107 coupled with UPLC-MS analysis, showed significantly reduced amidase activity in these mutants
108 compared to $TseP^N$ (Figure 2D).

109 To test the role of metal ions for TseP's amidase activity, we added the chelating agent EDTA to
110 the PG-digestion mixture, which abolished the amidase activity (Figure 2E). To further identify the
111 specific metal ion involved, we also purified TseP in the presence of EDTA and then supplemented it
112 with Zn^{2+}, Ca^{2+} and a combination of both. PG-digestion assays revealed that adding Zn^{2+}, but not Ca^{2+},
113 restored the amidase function (Figure 2E).

114 Given the dual functionality of TseP, we sought to determine if TsiP, known as the immunity
115 protein neutralizing the lysozyme activity, could inhibit the amidase, by mixing purified TsiP with TseP,
116 $TseP^N$, and $TseP^C$ in varying molar ratios. Enzymatic assays using purified PG showed that TsiP could
117 effectively inhibit both amidase activity and peptidoglycan hydrolysis activity of TseP, $TseP^N$ and $TseP^C$
118 (Figure 2F, Supplemental Figure S1). Additionally, pull-down assays showed that TsiP interacts with not
119 only $TseP^C$ but also $TseP^N$ (Figure 2G). Collectively, these results indicate that $TseP^N$ is a Zn^{2+}-dependent
120 amidase.

121 **Amidase activity is not required for T6SS assembly or lysozyme function**

122 To determine whether the amidase activity is important for the structural role of $TseP^N$, we
123 expressed these amidase-inactive mutants in the Δ*3eff* TssB-sfGFP mutant and tested T6SS-related
124 functions. Secretion analysis revealed that expression of $TseP^{H339A}$, but not the other mutants, restored
125 Hcp secretion similar to wild-type TseP (Figure 3A). As control, we examined the expression of these

126 TseP variants and found comparable signals in the cell lysates and secretion samples. Observations of
127 TssB-sfGFP sheath assembly in the Δ*3eff* TssB-sfGFP mutant further supported these findings, with the
128 $TseP^{H339A}$ strain showing dynamic assembly of T6SS similar to the strain expressing the wild-type
129 protein (Figure 3B, Supplemental Figure S2A). Further analysis through bacterial competition assays,
130 with *E. coli* MG1655 strain as prey, mirrored these results (Figure 3C). The expression of $TseP^{H339A}$ and
131 TseP showed comparable killing abilities while the expression of other mutants demonstrated severely
132 impaired killing activities as the T6SS defective Δ*3eff* (Figure 3C). Although it is unclear why the other
133 mutations failed to complement, the H339A amidase-inactive mutation exhibiting a similar
134 complementary role to wild type TseP suggests that the amidase activity is not required for T6SS
135 assembly.

136 Additionally, we tested whether there is any synergistic effect between amidase and the $TseP^{C}$-
137 mediated lysozyme activities by comparing PG degradation treated with TseP, $TseP^{C}$, and $TseP^{H339A}$.
138 Results showed that TseP exhibited higher activities than the $TseP^{C}$ alone, but there was no difference
139 between TseP and the $TseP^{H339A}$ mutant (Figure 3D, Supplemental Figure S2B). This indicates that
140 amidase and lysozyme activities can operate as independent modules within the protein.

141 **TseP homologs exhibit similar dual functions**

142 Homolog searching analysis reveals a broad distribution of TseP homologs across Gram-negative
143 bacteria (Figure 4A, Supplemental Figure S3). To examine the dual functionality of these homologs, we
144 selected two representative proteins that have not been previously characterized: AHA_1849 from
145 *Aeromonas hydrophila* which is a closely related homolog from the same genus, and PSPTO_5204 from
146 *Pseudomonas syringae*, a more distantly related homolog. To determine whether AHA_1849 and
147 PSPTO_5204 share amidase and lysozyme activities as TseP, we expressed and purified their respective
148 N- and C-terminal truncated mutants, AHA_1849^{N} (1-640aa), AHA_1849^{C} (641-851aa), $PSPTO_5204^{N}$
149 (1-343aa), and $PSPTO_5204^{C}$ (344-588aa) (Supplemental Figure S3). We also constructed inactivating
150 mutations in their predicted catalytic residues for each protein to serve as controls (Supplemental Figure

151 S3). Subsequent PG-hydrolysis and UPLC-MS analysis confirmed that both AHA_1849 and
152 PSPTO_5204 exhibit dual amidase and lysozyme activities, capable of cleaving both peptide and glycan
153 chains (Figure 4, B and C).

154 Additionally, by analyzing the GC-contents of the two *Aeromonas* homologs, we found that the
155 GC-content of $TseP^N$ is about 10% higher than that of $TseP^C$ and 10% lower than the upstream VgrG
156 (Figure 4D). This suggests that these two domains might have been horizontally transferred and
157 subsequently fused during evolution. To explore this hypothesis further, we searched for homolog
158 proteins with similar structures to either $TseP^N$ or $TseP^C$ in the Foldseek Search AFDB50 database (41),
159 yielding 1000 proteins with comparable predicted structures. We identified $TseP^N$-only homologs in
160 various *Aeromonas* species, including a specific homolog in *A. schubertii* possessing only the $TseP^N$
161 domain, whereas $TseP^C$-homologs were discovered in several other species, such as *Fulvimonas soli* and
162 *Vibrio campbellii* (Figure 4E). The comparison of their predicted structures reveals high similarity
163 (Figure 4F, Supplemental Table S2 and S3), further supporting the notion that $TseP^N$ and $TseP^C$ domains
164 may have been fused through a recombination event, resulting in a chimeric, dual-functional TseP.

165 **Crystallographic analysis of $TseP^C$ reveals a wide active groove**

166 While testing TseP-mediated hydrolysis of purified PG from Gram-negative bacteria, we noticed
167 that both TseP and $TseP^C$ displayed more efficient digestion than the commonly used hen-egg lysozyme
168 (Figure 5A). This enhanced activity suggests that TseP may utilize a unique mechanism for cell wall
169 degradation. To further investigate this, we determined the X-ray crystal structure of $TseP^C$ to a resolution
170 of 2.27Å (R_{work} =0.189 and R_{free}=0.227), by molecular replacement with one molecule in the asymmetric
171 unit (Table 1).

172 The crystal structure revealed that $TseP^C$ comprises a smaller lobe of seven helices and a larger
173 lobe of ten helices, separated by a concave groove (Figures 5B, Supplemental Figure S4A). The surface
174 electrostatic potential of $TseP^C$, calculated using the Adaptive Poisson-Boltzmann Solver (APBS),
175 consists of both electronegative and electropositive regions, unlike the predominantly electronegative

176 groove of lysozyme (Figure 5C, Supplemental Figure S4B). The electropositive surface of $TseP^{C}$ consists
177 of residues R723 and K796, with an adjacent residue Y720 corresponding to W62 in lysozyme, altering
178 which is known to affect substrate binding (42). Additionally, the previously predicted catalytic dyad
179 (E655 and E663) was located near the groove. Although this structural arrangement resembles that of
180 other lysozyme family members, $TseP^{C}$ exhibits a less compact conformation with a notably wider
181 groove compared to the typical lysozyme (Figure 5D). Previous studies have shown that the lysozyme
182 possesses catalytic sites at E53 and D70 in the substrate-binding groove (42), while the active residues
183 in the $TseP^{C}$ structure are E654 and E663, respectively (Figure 5D). To test the effect of E663 for $TseP^{C}$
184 activity, we purified a mutant E663D ($TseP^{C\text{-}E663D}$) protein and perform PG digestion assays. The results
185 show that $TseP^{C\text{-}E663D}$ lost the activity, suggesting the greater distance within the groove requires this
186 glutamate residue (Figure 5E). These results collectively highlight the key structural features that may
187 account for the increased activity of $TseP^{C}$ relative to the hen-egg lysozyme.

188 **Engineered $TseP^{C}$ can lyse Gram-positive cells**

189 To test whether TseP can degrade various cell walls, we purified PG from *B. subtilis*, a model
190 Gram-positive bacterium, for use as substrate. However, we failed to detect any PG hydrolysis treated
191 with TseP or $TseP^{C}$, in contrast to the lysozyme (Figure 6A). Further purification of PG with NaOH
192 treatment, removing PG-associated peptides, led to effective hydrolysis of PG by TseP and $TseP^{C}$,
193 suggesting a difference in substrate accessibility between the lysozyme and TseP. By comparing protein
194 surface electrostatic potentials between the lysozyme and $TseP^{C}$, we noticed a more electronegative
195 surface patch in $TseP^{C}$, suggesting a potential electrostatic repulsion from negatively charged PG (Figure
196 6B, Supplemental Figure S4B). To increase electropositive regions while minimizing impact on activity,
197 we mutated four negative charge residues distant from the active site and obtained a quadruple mutant
198 $TseP^{C4+}$ (Figure 6B). Activity assays confirmed that $TseP^{C4+}$ retained PG-hydrolyzing activities (Figure
199 6C). To test whether the engineered $TseP^{C4+}$ was able to lyse *B. subtilis*, we treated *B. subtilis* cells with
200 purified $TseP^{C}$ and $TseP^{C4+}$ and found that cells were lysed effectively by $TseP^{C4+}$ but not $TseP^{C}$ (Figure

201 6D, Supplemental Figure S4C). These results indicate that modulating the surface charge is an effective
202 strategy to expand the target range of PG-lysing effectors.

203 Next, we tested whether the engineered $TseP^{C4+}$ could be delivered by the T6SS for inhibiting *B.*
204 *subtilis*. Protein secretion analysis showed a significant $TseP^{C4+}$ signal in secretion samples, despite at a
205 lower level than the wild type $TseP^{C}$ (Figure 6E). When *B. subtilis* was co-incubated with the Δ*tseP*
206 mutant expressing the engineered $TseP^{C4+}$ in liquid culture, survival of *B. subtilis* was significantly
207 reduced in a T6SS-dependent manner (Figure 6F, Supplemental Figure S4D). These data collectively
208 suggest that the T6SS can be armed with engineered $TseP^{C4+}$ to gain Gram-positive killing capabilities
209 in a contact-independent manner.

210

211 **Discussion**

212 The T6SS plays a pivotal role in bacterial competition, using a variety of antibacterial effectors
213 to kill competing cells. The exploration of effector functions holds the promise of unlocking a largely
214 untapped source of novel antimicrobials, presenting innovative approaches to address the escalating
215 antimicrobial resistance crisis. Here we report that TseP represents a novel family of dual-functional
216 chimeric effectors, exhibiting both amidase and lysozyme activities. Our study reveals that the N-
217 terminus of TseP not only serves a critical structural role in T6SS assembly but also acts as a Zn^{2+}-
218 dependent amidase. The N- and C-domains are both secreted and functionally independent, and may be
219 subject to an evolutionary fusion event to form the chimeric full-length TseP. Such multifunctionality
220 underscores a complex evolutionary strategy aimed at promoting T6SS-mediated competitiveness.

221 Among the known T6SS effectors, those targeting the bacterial PG layer represent a prevalent
222 category. Certain T6SSs are capable of translocating multiple PG-targeting effectors. For instance, the
223 H1-T6SS in *Pseudomonas aeruginosa* deploys Tse1 and Tse3, while *Vibrio cholerae* secretes VgrG3
224 and TseH (5–7, 9, 43, 44). Tse1 and TseH exhibit endopeptidase activities, whereas Tse3 and VgrG3
225 have potent lysozyme activities (5–7, 9, 43, 44). Yet, it remains relatively uncommon to identify effectors

226 that possess dual functionality, capable of cleaving both the glycan chains and the cross-linked peptides
227 within the bacterial cell wall. To date, the sole established example is Tse4 from *A. baumannii*, which
228 acts both as a transglycosylase to cleave the glycan strand and as an endopeptidase to cut the peptide
229 cross-bridge (10, 45, 46). Our enzymatic assays reveal that TseP distinguishes itself from Tse4 with dual
230 roles as a lysozyme and an amidase, as well as a structural role for T6SS assembly. Further homology
231 searches and biochemical validations of homolog activities substantiate that TseP constitutes a new
232 family of dual-functional effectors.

233 Our data demonstrate that the N-terminus of TseP can modulate T6SS assembly, which provides
234 further evidence that effectors play a crucial structural role in T6SS assembly (23, 37, 47, 48). Although
235 this notion has now been shown in several species, the molecular details remain elusive. The assembly
236 of a non-contractile mutant T6SS in *V. cholerae* in the absence of effectors suggests that effectors might
237 be needed to stabilize a polymerizing T6SS (49). In comparison to $TseP^{C}$, the N-terminus not only
238 contributes to T6SS assembly but also exhibits 10% higher GC content. Additionally, both N and C-
239 terminus can be independently secreted by the T6SS. Using structure-assisted homolog search, we have
240 identified $TseP^{N}$ and $TseP^{C}$-only proteins in different species. These data suggest that these two domains
241 may result from independent effector proteins and have undergone an evolutionary fusion event.

242 Previous studies have shown that expressing TseP in the periplasm is highly toxic, but this
243 toxicity is mitigated when catalytic mutations are introduced into the C-terminal lysozyme domain (38).
244 This indicates that the N-terminal amidase is either less toxic or is tightly regulated by the concentration
245 of Zn^{2+} in the growth medium. Although the total intracellular Zn^{2+} concentration during growth in LB
246 has been reported to be around 0.1mM—approximately 100 times higher than the Zn^{2+} level in the LB
247 medium—the bioavailable (free) Zn^{2+} concentration within *E. coli* cells remains exceedingly low (50).
248 A similar dependency on metal ions was observed with another cell-wall-targeting endopeptidase
249 effector, TseH, whose activity is dependent on the environmental concentrations of Mg^{2+} and Ca^{2+} (51).

250 Such metal ion dependencies might lead to misbelief about these effectors being cryptic or inactive,
251 complicating the discovery and functional analysis of these important proteins.

252 TseP is predicted to contain an EF-hand calcium-binding domain with a "helix-loop-helix" motif,
253 a feature previously unreported in T6SS effectors (Supplemental Figure S5A). However, mutations
254 introduced to this domain, aimed at exploring its role in T6SS assembly and TseP toxicity, did not reveal
255 any critical effect on TseP functions under the conditions tested (Supplemental Figure S5, B and C). It is
256 possible that this EF-hand motif is active under more Ca^{2+} stringent conditions or during infections.
257 Further study is required to decipher its physiological function. Additionally, while constructing TseP
258 variants with different residue changes, we noticed that even single residue changes could reduce the
259 expression, secretion or the structural role of TseP, highlighting the technical challenge of heterologous
260 effector engineering (Figure 3A, Supplemental Figure S6, A and B).

261 Because the outer membrane of Gram-negative bacteria generally prohibits the entry of cell-wall
262 lysing proteins, the relatively exposed Gram-positive bacteria are likely more amenable to such
263 treatments. However, the T6SS, exclusively found in Gram-negative bacteria, primarily targets Gram-
264 negative species. To date, only two T6SSs, identified in *Acidovorax citrulli* and *A. baumannii* (10, 13),
265 have shown the capability to kill Gram-positive bacteria. Additionally, no Gram-positive cell wall lysing
266 effectors have been reported; for instance, Tse4 from *A. baumannii* cannot directly lyse *B. subtilis*
267 cultures but requires T6SS delivery. Our biochemical characterization and engineering of $TseP^{C}$ not only
268 establishes its exceptional enzymatic activity but also demonstrates an effective strategy to acquire Gram-
269 positive-cell lysing activities, as well as to equip the T6SS of *A. dhakensis* with a contact-independent
270 killing ability. These results highlight the potential of antimicrobial effector engineering in addressing
271 antimicrobial resistance.

272 In conclusion, our study unveils a new family of dual functional chimeric T6SS effectors and
273 demonstrates the potential for bioengineering these proteins to broaden their antimicrobial spectrum. The
274 engineered $TseP^{C}$ represents the first effector variant capable of directly lysing *B. subtilis* cultures, paying

275 the way for engineering the diverse set of T6SS cell-wall targeting effectors. The urgent need for new
276 antimicrobials necessitates the exploration of innovative strategies. The insights from our research into
277 T6SS and its diverse effectors signal promising directions for future work in microbial biology and
278 antimicrobial therapy. When enhanced through protein engineering, these enzymes have the potential to
279 address bacterial infections not only in medical settings but also in food safety and animal health.

280 **Materials and Methods**

281 **Bacterial strains and growth conditions**

282 All strains and plasmids used in this study are displayed in Supplemental Table S1. Strains were routinely
283 cultivated in Lysogeny Broth (LB) ([w/v] 1% tryptone, 0.5% yeast extract, 0.5% NaCl) under aerobic
284 conditions at 37 °C. Antibiotics were supplemented at the following concentrations: streptomycin (100
285 μg/ml), kanamycin (50 μg/ml), gentamicin (20 μg/ml), chloramphenicol (25 μg/ml for *E. coli*, 2.5 μg/ml
286 for SSU). All plasmids were constructed using standard molecular techniques, and their sequences were
287 verified through Sanger sequencing. All strains and plasmids are available upon request.

288 **Protein secretion assay**

289 Secretion assays were performed as previously described (38). Briefly, cells were grown in LB to
290 OD_{600}=1 and collected by centrifugation at 2,500 × *g*. The pellets were resuspended in fresh LB and
291 incubated at 28 °C for 2 h with 0.01% (w/v) L-arabinose. After incubation, cells were pelleted again by
292 centrifugation at 2,500 × *g* for 8 min. Cell pellets were then resuspended in SDS-loading dye and used
293 as cell lysate samples. The supernatants were centrifuged again at 12,000 × *g* for 30 s and then
294 precipitated in 10% (v/v) TCA (trichloroacetic acid) at -20 °C for 30 min. Precipitated proteins were
295 collected by centrifugation at 15,000 × *g* for 30 min at 4 °C, and then washed twice with acetone. The
296 air-dried pellets were resuspended in SDS-loading dye and used as the secreted protein samples. All the
297 samples were boiled for 10 min before SDS-PAGE analysis.

298 **Western blotting analysis**

299 Proteins were separated using SDS-PAGE and subsequently transferred onto a PVDF membrane (Bio-
300 Rad). Prior to antibody incubation, the membrane was blocked with a solution of 5% (w/v) non-fat milk
301 dissolved in TBST buffer (consisting of 50 mM Tris, 150 mM NaCl, 0.1% [v/v] Tween-20, pH 7.6) for
302 1 h at room temperature. The membrane was then incubated sequentially with primary and secondary
303 antibodies. The Clarity ECL solution (Bio-Rad) was utilized for signal detection. Monoclonal antibodies
304 specific to RpoB (RNA polymerase beta subunit) were sourced from Biolegend (Product # 663905).
305 Additionally, polyclonal antibodies to Hcp were customized by Shanghai Youlong Biotech (39). HRP-
306 linked secondary antibodies were purchased from Beyotime Biotechnology (Product # A0208 and #
307 A0216, respectively).

308 **Protein expression and purification**

309 Proteins were expressed using pET28a vector with the His tag in *E. coli* BL21 (DE3). Strains containing
310 the recombinant plasmid were grown in LB at 37 °C. When the optical density of the culture reached
311 OD_{600} of 0.6, isopropyl-β-D-thiogalactopyranoside (IPTG) was added to a final concentration of 1 mM,
312 and the culture was incubated at 20 °C for 16 h. The cells were collected by centrifugation at 2,500 × *g*
313 for 10 minutes at 4°C, resuspended in lysis buffer (20 mM Tris-HCl, 300 mM NaCl, 10 mM imidazole,
314 pH 8.0), and lysed by sonication. After sonication, the lysate was centrifuged at 12,000 × *g* for 60 min at
315 4 °C, and the supernatant was collected. Ni-NTA affinity chromatography was used to purify the target
316 protein, followed by gel filtration using Superdex 200 pg 10/300 column (GE Healthcare). The protein
317 was finally concentrated to 15 mg/ml. All samples were visualized by SDS-PAGE and stained with
318 Coomassie brilliant blue dye. Gel images for all purified proteins used in this study are shown in
319 Supplemental Figure S7.

320 **Crystallization, X-ray data collection and structure determination**

321 $TseP^C$ was crystallized at 18 °C using the hanging drop method. Equal volumes (1:1) of the protein
322 solution and reservoir solution, containing 0.1 M sodium formate (pH 7.0) and 12% (w/v) PEG 3350,

323 were mixed. The crystals were cryoprotected in a mother liquor containing 20% v/v glycol and were
324 flash-cooled at 100 K.
325 An X-ray diffraction data set of $TseP^C$ was collected at beamline BL19U1 (wavelength, 0.97852 Å) at
326 the Shanghai Synchrotron Radiation Facility. Diffraction data was auto-processed by an aquarium
327 pipeline. The crystals were diffracted to 2.27 Å and belonged to the space group C 2 2 21 with unit cell
328 dimensions of a = 44.48 Å, b = 138.8 Å and c = 95.83 Å. This structure was solved by molecular
329 replacement with PHASER using the previously reported SPN1S endolysin structure (PDB ID: 4OK7)
330 as the searching model and further polished by COOT and PHENIX. refine (52, 53). All structure figures
331 were generated using PyMOL (https://pymol.org/2/) software (54).
332 **Peptidoglycan purification**
333 Peptidoglycan was extracted as previously described (55). Bacteria were cultured at 37 °C for 8 h. Cells
334 were then centrifuged at 4 °C for 30 min at 3,000 × *g* and the cell pellets were washed with ultrapure
335 water. After washing, the bacteria were resuspended in ultrapure water to an OD_{600} of 70-100 and then
336 added dropwise to an equal volume of boiling 8% SDS solution. The mixture was slowly stirred while
337 boiling for 3 h and then cooled naturally to room temperature. The precipitate was collected at 20 °C for
338 1 h at 100,000 × *g* and washed with ultrapure water five times. To remove the residual proteins and DNA,
339 the precipitate was resuspended in 10 ml of 10 mM Tris-HCl (pH 7.0) and treated with 5 mg DNase I
340 and 16 mg trypsin at 37 °C for 16 h. After treatment, the mixture was centrifuged at room temperature
341 for 1 h at 100,000 × *g*, and the pellets were dissolved and treated with an equal volume of boiling 8%
342 SDS solution for another 3 h. The purified peptidoglycan was obtained after washing with ultrapure water,
343 freeze-dried, and stored at -20℃.
344 ***In vitro* enzymatic assays and enzyme kinetics**
345 To characterize the *in vitro* enzymatic activity of TseP and its homologs, 500 μg of purified *E. coli* PG
346 was co-incubated with an equal amount of proteins in a 0.1 ml reaction system at 37 °C for 12 h. After
347 centrifugation, the supernatant was collected and subjected to analysis by ultraperformance liquid

348 chromatography-quadrupole time of flight mass spectrometry (UPLC-QTOF-MS). The Acquity UPLC
349 HSS T3 column was chosen as the solid phase, with solvent A (water with 0.1% [v/v] formic acid) and
350 solvent B (methanol) as the mobile phase. Analyte separation was achieved by a linear gradient of solvent
351 B, which was gradually increased from 1% to 20% over 65 min. Thereafter, a rapid gradient adjustment
352 was followed to increase the concentration of solvent B from 20% to 100% in 1 min, with a retention
353 period of 5 min to ensure complete separation. Finally, the system was flushed with 99% solvent A for
354 4 min to complete the process.
355 To measure the enzyme kinetics of $TseP^{C}$, a dye-release method was used to detect the PG hydrolyzing.
356 Prior to use, the purified PG was labelled by Remazol Brilliant Blue (RBB) following a previously
357 described method (56). Briefly, purified PG was incubated with 20 mM RBB in 0.25 M NaOH for 12 h
358 at 37°C. The RBB-labelled PG was collected via centrifugation for 10 min at 21,400 × *g* and washed
359 with ultrapure water several times until no RBB dye could be detected in the supernatant. This RBB-
360 labelled PG was then applied for the enzyme kinetics analysis. In each reaction, 10 nM enzyme was
361 mixed with different concentrations of RBB-labelled PG at 37°C for 10 min. Undigested PG was pelleted
362 by centrifugation at 21,400 × *g* for 10 min and the dye release in the supernatant was quantified by
363 measuring its absorbance at OD_{595}.
364 **Bacterial competition assays**
365 Killer and prey strains were grown aerobically in liquid LB medium until they reached OD_{600} values of
366 1 and 2, respectively. Later, the cells were harvested via centrifugation and gently resuspended in fresh
367 LB broth. Killer and prey cells mixed at a ratio of 5:1 were deposited onto LB-agar plates supplemented
368 with 0.01% (w/v) L-arabinose and co-incubated for 6 h at 28°C. Afterward, the mixed cells were
369 recovered in fresh LB broth and vigorously vortexed to dislodge the agar. For the Gram-positive bacterial
370 killing, the SSU and *B. subtilis* cells were mixed at a ratio of 20:1 with 0.01% L-arabinose in liquid LB
371 medium for 24 h at 28°C. The mixtures were then serially diluted and plated onto specific antibiotic-
372 containing plates.

373 **Bioinformatics analysis**

374 The gene sequences of *A. dhakensis* SSU were retrieved from the draft genome assembly (GenBank
375 accession NZ_JH815591.1) and confirmed by Sanger sequencing. The resulting sequences were then
376 aligned using Clustal Omega (57), and the alignment was visualized using ESPript with its default
377 settings (https://espript.ibcp.fr)(58).

378 **Data availability**

379 The data that support the findings of this study are available within the article or from the corresponding
380 author upon reasonable request.

381 **Protein Data Bank and accession code**

382 The atomic coordinate and structure factor of $TseP^C$ have been deposited in the Protein Data Bank with
383 accession code 8XCL.

384 **Acknowledgements**

This work was supported by funding from National Natural Science Foundation of China (32030001) and National Key R&D Program of China (2020YFA0907200). The funders had no role in study design, data collection and interpretation, or the decision to submit the work for publication.

385 **Author contributions**

T.D. conceived the project. Z-H.W., T-T.P., D.Y.W., and X.L. performed research and data analysis. Z--H.W., Y.A., T.Z., and W.Q. performed the crystallography and structural analysis. T.D. and Z-H.W.. wrote the manuscript with assistance from Y.A.

Competing interests
The authors declare no competing interests.

References

1. C. J. L. Murray, *et al.*, Global burden of bacterial antimicrobial resistance in 2019: a systematic analysis. *The Lancet* **399**, 629–655 (2022).
2. J. O'Neill, Tackling drug-resistant infections globally: final report and recommendations. *Wellcome Collect.* (2016). Available at: https://wellcomecollection.org/works/thvwsuba/items.

3. R. A. Bonomo, β-lactamases: a focus on current challenges. *Cold Spring Harb. Perspect. Med.* **7**, a025239 (2017).
4. S. M. Drawz, R. A. Bonomo, Three decades of β-lactamase inhibitors. *Clin. Microbiol. Rev.* **23**, 160–201 (2010).
5. T. M. Brooks, D. Unterweger, V. Bachmann, B. Kostiuk, S. Pukatzki, Lytic activity of the *Vibrio cholerae* type VI secretion toxin VgrG-3 is inhibited by the antitoxin TsaB. *J. Biol. Chem.* **288**, 7618–7625 (2013).
6. T. G. Dong, B. T. Ho, D. R. Yoder-Himes, J. J. Mekalanos, Identification of T6SS-dependent effector and immunity proteins by Tn-seq in *Vibrio cholerae*. *Proc. Natl. Acad. Sci. U. S. A.* **110**, 2623–2628 (2013).
7. A. B. Russell, *et al.*, Type VI secretion delivers bacteriolytic effectors to target cells. *Nature* **475**, 343–347 (2011).
8. J. C. Whitney, *et al.*, A broadly distributed toxin family mediates contact-dependent antagonism between gram-positive bacteria. *eLife* **6**, e26938 (2017).
9. R. D. Hood, *et al.*, A type VI secretion system of *Pseudomonas aeruginosa* targets a toxin to bacteria. *Cell Host Microbe* **7**, 25–37 (2010).
10. N.-H. Le, V. Pinedo, J. Lopez, F. Cava, M. F. Feldman, Killing of Gram-negative and Gram-positive bacteria by a bifunctional cell wall-targeting T6SS effector. *Proc. Natl. Acad. Sci. U. S. A.* **118**, e2106555118 (2021).
11. A. T. Ma, S. McAuley, S. Pukatzki, J. J. Mekalanos, Translocation of a *Vibrio cholerae* type VI secretion effector requires bacterial endocytosis by host cells. *Cell Host Microbe* **5**, 234–243 (2009).
12. J. D. Mougous, *et al.*, A virulence locus of *Pseudomonas aeruginosa* encodes a protein secretion apparatus. *Science* **312**, 1526–1530 (2006).
13. T.-T. Pei, *et al.*, Delivery of an Rhs-family nuclease effector reveals direct penetration of the gram-positive cell envelope by a type VI secretion system in *Acidovorax citrulli*. *mLife* **1**, 66–78 (2022).
14. S. Pukatzki, *et al.*, Identification of a conserved bacterial protein secretion system in *Vibrio cholerae* using the *Dictyostelium* host model system. *Proc. Natl. Acad. Sci. U. S. A.* **103**, 1528–1533 (2006).
15. K. Trunk, *et al.*, The type VI secretion system deploys antifungal effectors against microbial competitors. *Nat. Microbiol.* **3**, 920–931 (2018).
16. M. Basler, M. Pilhofer, P. G. Henderson, J. G. Jensen, J. Mekalanos, Type VI secretion requires a dynamic contractile phage tail-like structure. *Nature* **483**, 182–186 (2012).
17. Y. R. Brunet, A. Zoued, F. Boyer, B. Douzi, E. Cascales, The type VI secretion TssEFGK-VgrG phage-like baseplate is recruited to the TssJLM membrane complex via multiple contacts and serves as assembly platform for tail tube/sheath polymerization. *PLoS Genet.* **11**, e1005545 (2015).
18. B. T. Ho, T. G. Dong, J. J. Mekalanos, A view to a kill: the bacterial type 6 secretion system. *Cell Host Microbe* **15**, 9–21 (2014).
19. J. Wang, M. Brodmann, M. Basler, Assembly and subcellular localization of bacterial type VI secretion systems. *Annu. Rev. Microbiol.* **73**, 621–638 (2019).
20. S. Pukatzki, *et al.*, Identification of a conserved bacterial protein secretion system in *Vibrio cholerae* using the *Dictyostelium* host model system. *Proc. Natl. Acad. Sci. U. S. A.* **103**, 1528–1533 (2006).
21. M. M. Shneider, *et al.*, PAAR-repeat proteins sharpen and diversify the type VI secretion system spike. *Nature* **500**, 350–353 (2013).
22. F. Kamal, *et al.*, Differential cellular response to translocated toxic effectors and physical penetration by the type VI secretion system. *Cell Rep.* **31**, 107766 (2020).
23. X. Liang, *et al.*, An onboard checking mechanism ensures effector delivery of the type VI secretion system in *Vibrio cholerae*. *Proc. Natl. Acad. Sci. U. S. A.* **116**, 23292–23298 (2019).
24. A. Vettiger, M. Basler, Type VI secretion system substrates are transferred and reused among sister cells. *Cell* **167**, 99-110.e12 (2016).
25. X. Liang, *et al.*, Identification of divergent type VI secretion effectors using a conserved chaperone domain. *Proc. Natl. Acad. Sci. U. S. A.* **112**, 9106–9111 (2015).
26. S. Pukatzki, A. T. Ma, A. T. Revel, D. Sturtevant, J. J. Mekalanos, Type VI secretion system translocates a phage tail spike-like protein into target cells where it cross-links actin. *Proc. Natl. Acad. Sci. U. S. A.* **104**, 15508–15513 (2007).
27. A. B. Russell, *et al.*, A widespread bacterial type VI secretion effector superfamily identified using a heuristic approach. *Cell Host Microbe* **11**, 538–549 (2012).

28. D. Salomon, *et al.*, Marker for type VI secretion system effectors. *Proc. Natl. Acad. Sci. U. S. A.* **111**, 9271–9276 (2014).
29. M. Si, *et al.*, Manganese scavenging and oxidative stress response mediated by type VI secretion system in *Burkholderia thailandensis*. *Proc. Natl. Acad. Sci. U. S. A.* **114**, E2233–E2242 (2017).
30. J. C. Whitney, *et al.*, An interbacterial NAD(P)$^+$ glycohydrolase toxin requires elongation factor Tu for delivery to target cells. *Cell* **163**, 607–619 (2015).
31. W. Vollmer, D. Blanot, M. A. De Pedro, Peptidoglycan structure and architecture. *FEMS Microbiol. Rev.* **32**, 149–167 (2008).
32. J. Ma, M. Sun, Z. Pan, C. Lu, H. Yao, Diverse toxic effectors are harbored by *vgrG* islands for interbacterial antagonism in type VI secretion system. *Biochim. Biophys. Acta BBA - Gen. Subj.* **1862**, 1635–1643 (2018).
33. R. E. Hernandez, R. Gallegos-Monterrosa, S. J. Coulthurst, Type VI secretion system effector proteins: Effective weapons for bacterial competitiveness. *Cell. Microbiol.* **22**, e13241 (2020).
34. J. C. Whitney, *et al.*, Identification, structure, and function of a novel type VI secretion septidoglycan glycoside hydrolase effector-immunity pair. *J. Biol. Chem.* **288**, 26616–26624 (2013).
35. P.-L. Chen, B. Lamy, W.-C. Ko, *Aeromonas dhakensis*, an increasingly recognized human pathogen. *Front. Microbiol.* **7**, 793 (2016).
36. H. Kitagawa, *et al.*, *Aeromonas dhakensis* is not a rare cause of *Aeromonas* bacteremia in Hiroshima, Japan. *J. Infect. Chemother.* **26**, 316–320 (2020).
37. X. Liang, *et al.*, VgrG spike dictates PAAR requirement for the assembly of the type VI secretion system. *J. Bacteriol.* e0035622 (2023). https://doi.org/10.1128/jb.00356-22.
38. X. Liang, *et al.*, Characterization of lysozyme-like effector TseP reveals the dependence of type VI secretion system (T6SS) secretion on effectors in *Aeromonas dhakensis* strain SSU. *Appl. Environ. Microbiol.* **87**, e0043521 (2021).
39. T.-T. Pei, *et al.*, Intramolecular chaperone-mediated secretion of an Rhs effector toxin by a type VI secretion system. *Nat. Commun.* **11**, 1865 (2020).
40. G. Suarez, *et al.*, Molecular characterization of a functional type VI secretion system from a clinical isolate of *Aeromonas hydrophila*. *Microb. Pathog.* **44**, 344–361 (2008).
41. M. van Kempen, *et al.*, Fast and accurate protein structure search with Foldseek. *Nat. Biotechnol.* **42**, 243–246 (2024).
42. K. Maenaka, *et al.*, Dissection of protein-carbohydrate interactions in mutant hen egg-white lysozyme complexes and their hydrolytic activity. *J. Mol. Biol.* **247**, 281–293 (1995).
43. E. Altindis, T. Dong, C. Catalano, J. Mekalanos, Secretome analysis of *Vibrio cholerae* type VI secretion system reveals a new effector-immunity pair. *mBio* **6**, e00075 (2015).
44. S. J. Hersch, *et al.*, Envelope stress responses defend against type six secretion system attacks independently of immunity proteins. *Nat. Microbiol.* **5**, 706–714 (2020).
45. S. Chou, *et al.*, Structure of a peptidoglycan amidase effector targeted to Gram-negative bacteria by the type VI secretion system. *Cell Rep.* **1**, 656–664 (2012).
46. A. Radkov, *et al.*, Antibacterial potency of type VI amidase effector toxins is dependent on substrate topology and cellular context. *eLife* **11**, e79796 (2022).
47. X. Liang, *et al.*, VgrG-dependent effectors and chaperones modulate the assembly of the type VI secretion system. *PLOS Pathog.* **17**, e1010116 (2021).
48. C.-F. Wu, *et al.*, Effector loading onto the VgrG carrier activates type VI secretion system assembly. *EMBO Rep.* **21**, e47961 (2019).
49. M. S. Stietz, X. Liang, H. Li, X. Zhang, T. G. Dong, TssA–TssM–TagA interaction modulates type VI secretion system sheath-tube assembly in *Vibrio cholerae*. *Nat. Commun.* **11** (2020).
50. C. E. Outten, and T. V. O'Halloran, Femtomolar sensitivity of metalloregulatory proteins controlling zinc homeostasis. *Science* **292**, 2488–2492 (2001).
51. M.-X. Tang, *et al.*, Abiotic factors modulate interspecies competition mediated by the type VI secretion system effectors in *Vibrio cholerae*. *ISME J.* **16**, 1765–1775 (2022).
52. P. D. Adams, *et al.*, PHENIX: building new software for automated crystallographic structure determination. *Acta Crystallogr. D Biol. Crystallogr.* **58**, 1948–1954 (2002).
53. P. Emsley, K. Cowtan, Coot: model-building tools for molecular graphics. *Acta Crystallogr. D Biol. Crystallogr.* **60**, 2126–2132 (2004).

54. Schrödinger, LLC, The PyMOL molecular graphics system, Version 1.8. (2015).
55. B. Glauner, Separation and quantification of muropeptides with high-performance liquid chromatography. *Anal. Biochem.* **172**, 451–464 (1988).
56. L. Yang, Y. Gan, L. Yang, B. Jiang, J. Tang, Peptidoglycan hydrolysis mediated by the amidase AmiC and its LytM activator NlpD is critical for cell separation and virulence in the phytopathogen *Xanthomonas campestris*. *Mol. Plant Pathol.* **19**, 1705–1718 (2018).
57. F. Sievers, *et al.*, Fast, scalable generation of high-quality protein multiple sequence alignments using Clustal Omega. *Mol. Syst. Biol.* **7**, 539 (2011).
58. X. Robert, P. Gouet, Deciphering key features in protein structures with the new ENDscript server. *Nucleic Acids Res.* **42**, W320–W324 (2014).
59. K. R. Park, *et al.*, Structural mechanism underlying regulation of human EFhd2/Swiprosin-1 actin-bundling activity by Ser183 phosphorylation. *Biochem. Biophys. Res. Commun.* **483**, 442–448 (2017).

Correspondence and request for materials should be addressed to T. Dong.

Figure legends

Figure 1. Structural roles and independent secretion of TseP domains. A, Secretion analysis of TseP, $TseP^N$, and $TseP^C$ in the SSU triple effector deletion mutant (Δ*3eff*). A schematic of the TseP N-terminus ($TseP^N$, 1-603 aa) and C-terminus ($TseP^C$, 604-845 aa) is depicted at the top. Hcp serves as a positive control for T6SS secretion. Hcp, RpoB, and 3V5-tagged TseP proteins were detected using specific antibodies. **B,** Time-lapse imaging of VipA-sfGFP signals in the Δ*3eff* mutant complemented with different TseP variants. Each sample was captured every 10 s for 5 min and temporally color-coded. Color scale used to temporally color code the VipA-sfGFP signals is shown at the bottom. A 30- × 30-μm representative field of cells is shown. Scale bars, 5 μm. **C,** Statistical analysis of T6SS sheath assemblies in the Δ*3eff* mutant complemented with different TseP variants. Error bars indicate the mean ± standard deviation of three biological replicates, and statistical significance was calculated using a two-tailed Student's *t*-test. ns, not significant; **, $P<0.01$. **D,** Secretion analysis of TseP, $TseP^N$, and $TseP^C$ in SSU wild type, Δ*vasK*, Δ*tseP*, and Δ*3eff* mutants. For **B** and **D**, TseP, $TseP^N$, and $TseP^C$ were tagged with a 3V5 C-terminal tag and expressed on pBAD vectors. RpoB serves as an equal loading and autolysis control. **E,** Pull-down analysis of VgrG2 with TseP, $TseP^N$, and $TseP^C$. His-tagged VgrG2 and 3V5-tagged TseP, $TseP^N$, or $TseP^C$ were used. His-tagged sfGFP and 3V5-tagged MBP were used as controls.

Figure 2. Functional analysis of TseP reveals an amidase activity. A, *In vitro* amidase activity of the TseP, $TseP^N$, $TseP^C$, and the lysozyme inactivated mutants $TseP^{E663A}$ and $TseP^{C\text{-}E663A}$. Cell-wall digestion products after incubation with the TseP or its mutants were analyzed by the UPLC/MS. **B,** MS analysis of cell-wall digestion products (NAM-NAC, tetrapeptides, and tripeptides) following treatment with TseP. **C,** Protein sequence alignment of the TseP amidase domain with other amidase homologs (top), and the structural superimposition of the TseP amidase domain and 3SLU (bottom). Cartoon representations of TseP and 3SLU are shown in green and cyan, respectively. The key residues involved in Zn^{2+} binding are shown in a stick model, and the zinc ion is indicated by the green sphere. **D,** *In vitro* amidase activity of $TseP^N$ and its amidase site mutated variants. **E,** *In vitro* amidase activity of TseP under cationic conditions of 2 mM EDTA, Zn^{2+}, Ca^{2+}, or a combination of both cations. TseP represents protein purified without EDTA treatment while $TseP^{EDTA}$ refers to protein purified in presence of EDTA. **F,** PG digestion analysis of $TseP^N$ with or without TsiP. The immunity protein TsiP was incubated with $TseP^N$ on ice for 12 h before being mixed with PG. Products in **D**, **E**, and **F** were analyzed by

UPLC-QTOF MASS. **G,** Pull-down analysis of TsiP with TseP, $TseP^N$, and $TseP^C$. His-tagged TsiP and 3V5-tagged TseP, $TseP^N$, or $TseP^C$ were used. His-tagged sfGFP and 3V5-tagged MBP were used as controls.

Figure 3. Amidase activity of TseP is not essential for T6SS assembly or lysozyme function. A, Secretion analysis of Hcp in the Δ*3eff* mutant complemented with different TseP variants. RpoB serves as an equal loading and autolysis control. Hcp, RpoB, and 3V5-tagged TseP proteins were detected using specific antibodies. **B,** Time-lapse imaging of VipA-sfGFP signals in the Δ*3eff* mutant complemented with TseP or its amidase-inactive mutant $TseP^{H339A}$. Each sample was captured every 10 s for 5 min and temporally color-coded. Color scale used to temporally color code the VipA-sfGFP signals is shown at the right. A 30 × 30 μm representative field of cells is shown. Scale bars, 5 μm. **C,** Competition analysis of the Δ*3eff* mutant complemented with different TseP variants. Competition assays were repeated once. **D,** Enzymatic activity of the TseP, $TseP^C$ and amidase-inactive mutant $TseP^{H339A}$. The error bars indicate the mean ± standard deviation of three biological replicates.

Figure 4. TseP homologs showed the same *in vitro* PG-hydrolysis activity with the TseP. A, Maximum-likelihood phylogeny of TseP homologs. Phylogeny was constructed using the IQ-tree web server with bootstrap 1000 times. Proteins tested in this study are highlighted in red. **B,** Amidase activity analysis of TseP homologs. **C,** *In vitro* PG-hydrolysis activity of the TseP homologs. Products in **B** and **C** were analyzed through UPLC-QTOF MASS. **D,** GC contents of the *tseP* gene cluster and *AHA_1849* gene cluster. **E,** Summary of $TseP^N$ and $TseP^C$ homologs output by Foldseek Search server. **F,** Structure alignments of TseP and homologs WL1483_2262 and DSB67_24810.

Figure 5. Crystal structure of $TseP^C$. A, Enzymatic activity of TseP, $TseP^C$, and lysozyme in hydrolyzing purified *E. coli* PG. The error bars indicate the mean standard deviation of three biological replicates. **B,** The overall structure of the $TseP^C$. The small lobe and large lobe are shown in cyan and green, respectively, with the connecting loop depicted in red. **C,** Electrostatic potential maps of $TseP^C$ with the Y720, R723, and K796 shown as a stick model. The electrostatic surface potentials are colored red for negative charges, blue for positive charges, and white for neutral residues. **D,** Structural comparison of $TseP^C$ and lysozyme (PDB ID: 1LZC). The catalytic sites are shown as a stick model. **E,** *E. coli* PG digestion analysis of $TseP^C$ and $TseP^{C\text{-}E663D}$ mutant. Error bars indicate the mean ± standard deviation of three biological replicates, and statistical significance was calculated using a two-tailed Student's *t*-test. ****, $P<0.0001$.

Figure 6. Modification of surface charge enables TseP^{C} to kill Gram-positive bacteria. A, *B. subtilis* PG digestion analysis of TseP and TseP^{C}. PG was treated with 0.25 M NaOH for 12 h at 37 °C to remove cross-linked peptides and teichoic acid. The lysis percentage was calculated by detecting the changes of OD_{600} during 1 h. The hen-egg lysozyme was used as a positive control. **B,** Electrostatic potential maps of the TseP^{C} and TseP^{C4+}. The active sites and the mutation region are highlighted in red circles. The negatively charged residues D604, E609, D841, and E845 in the mutation region are shown as a stick model and colored in green, and lysines are colored in cyan. **C,** *In vitro* PG-hydrolysis activity of the TseP^{C} and TseP^{C4+}. RBB-labelled *E. coli* PG was used as the substrate and the lysis percentage was detected by dye release. **D,** *B. subtilis* PG digestion analysis of TseP^{C} and TseP^{C4+}. Exponential phase *B. subtilis* cells (OD_{600}~1.0) were used as substrate. The lysis percentage was calculated by detecting the changes of OD_{600} during 1 h with the enzyme concentration at 100 nM. **E,** Secretion analysis of TseP^{C} and TseP^{C4+} in the Δ*tseP* mutant. RpoB serves as an equal loading and autolysis control. RpoB and 3V5-tagged TseP^{C} proteins were detected using specific antibodies. **F,** Statistical analysis of *B. subtilis* cells in the competition assays. Error bars of statistical analysis in **A**, **C**, **D**, and **F** indicate the mean ± standard deviation of three biological replicates, and statistical significance was calculated using a two-tailed Student's *t*-test. ns, not significant; *, $P<0.05$; **, $P<0.01$; ****, $P<0.0001$.

Figure 7. Model of TseP dual functions and engineering. This schematic illustrates the dual amidase-lysozyme activities of TseP and demonstrates an effective engineering strategy to enhance T6SS and its effector capabilities. The T6SS can independently secrete both the N- and C-terminal domains, with multiple evidence suggesting an evolutionary fusion event. These domains interact directly with the upstream-encoded carrier protein VgrG2 for secretion. TseP^{N}, the N-terminal domain, functions as a Zn^{2+}-dependent amidase, while the C-terminal domain, TseP^{C}, exhibits lysozyme activities. However, in its native form, TseP^{C} does not lyse Gram-positive *B. subtilis* cells. Through structural-guided design, TseP^{C} was engineered to create TseP^{C4+} by altering its surface charge. This modification enables TseP^{C4+} to lyse *B. subtilis* cells without affecting its T6SS-dependent secretion. Consequently, the T6SS-equipped cell acquires the ability to lyse *B. subtilis* in a contact-independent manner. Given the diversity of TseP-like effectors and T6SS species, this approach holds significant potential for modulating interspecies competition and combating antimicrobial resistance.

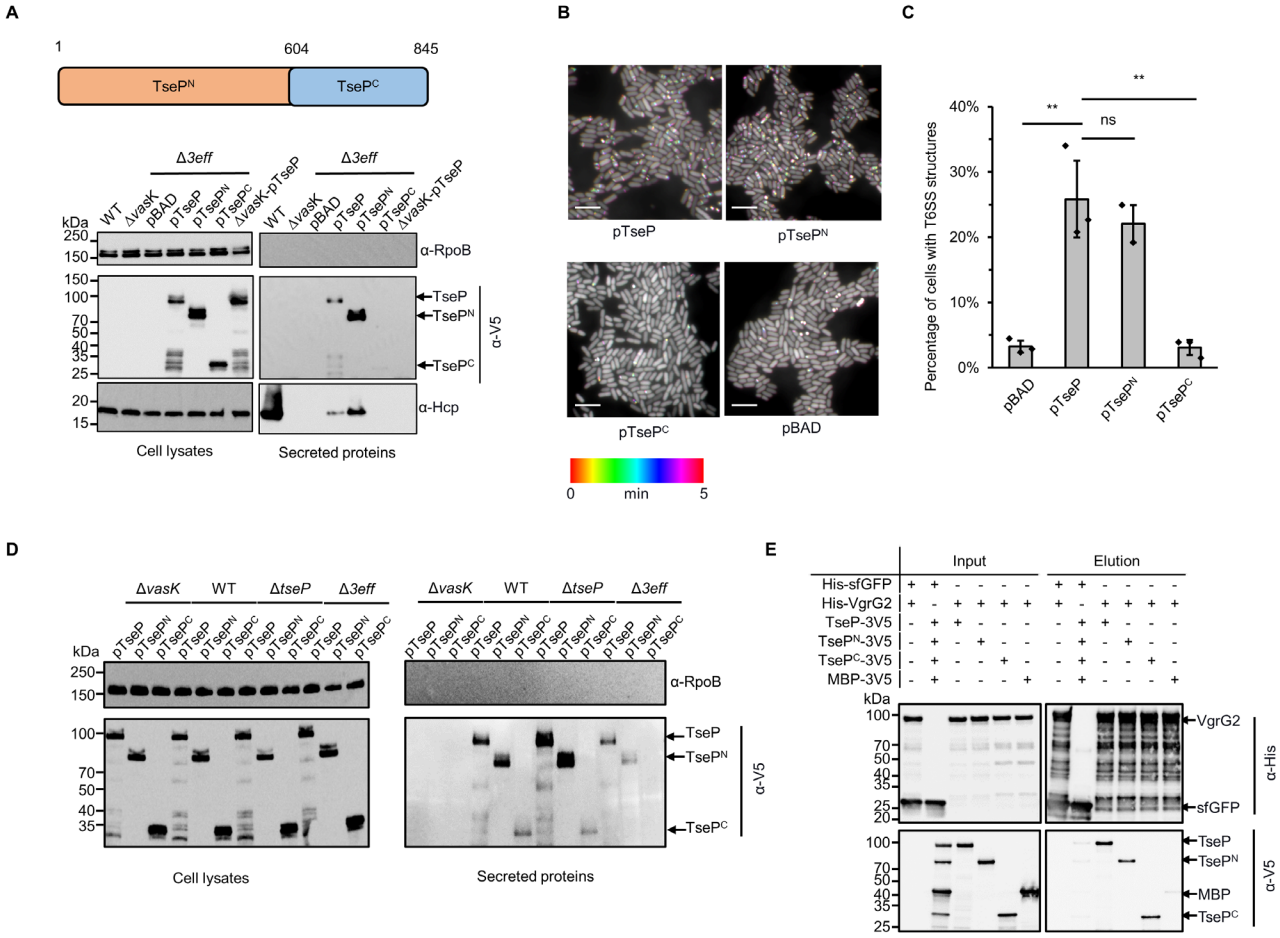
A
1
604
845
TseP^N
TseP^C
Δ3eff
Δ3eff
WT
ΔvasK
pBAD
pTseP
pTseP^N
pTseP^C
ΔvasK-pTseP
kDa
α-RpoB
α-V5
TseP
TseP^N
TseP^C
α-Hcp
Cell lysates
Secreted proteins
B
pTseP
pTseP^N
pTseP^C
pBAD
0
min
5
C
Percentage of cells with T6SS structures
40%
30%
20%
10%
0%
**
ns
**
pBAD
pTseP
pTseP^N
pTseP^C
D
ΔvasK
WT
ΔtseP
Δ3eff
α-RpoB
α-V5
Cell lysates
Secreted proteins
E
Input
Elution
His-sfGFP
His-VgrG2
TseP-3V5
TseP^N-3V5
TseP^C-3V5
MBP-3V5
VgrG2
sfGFP
α-His
TseP
TseP^N
MBP
TseP^C
α-V5

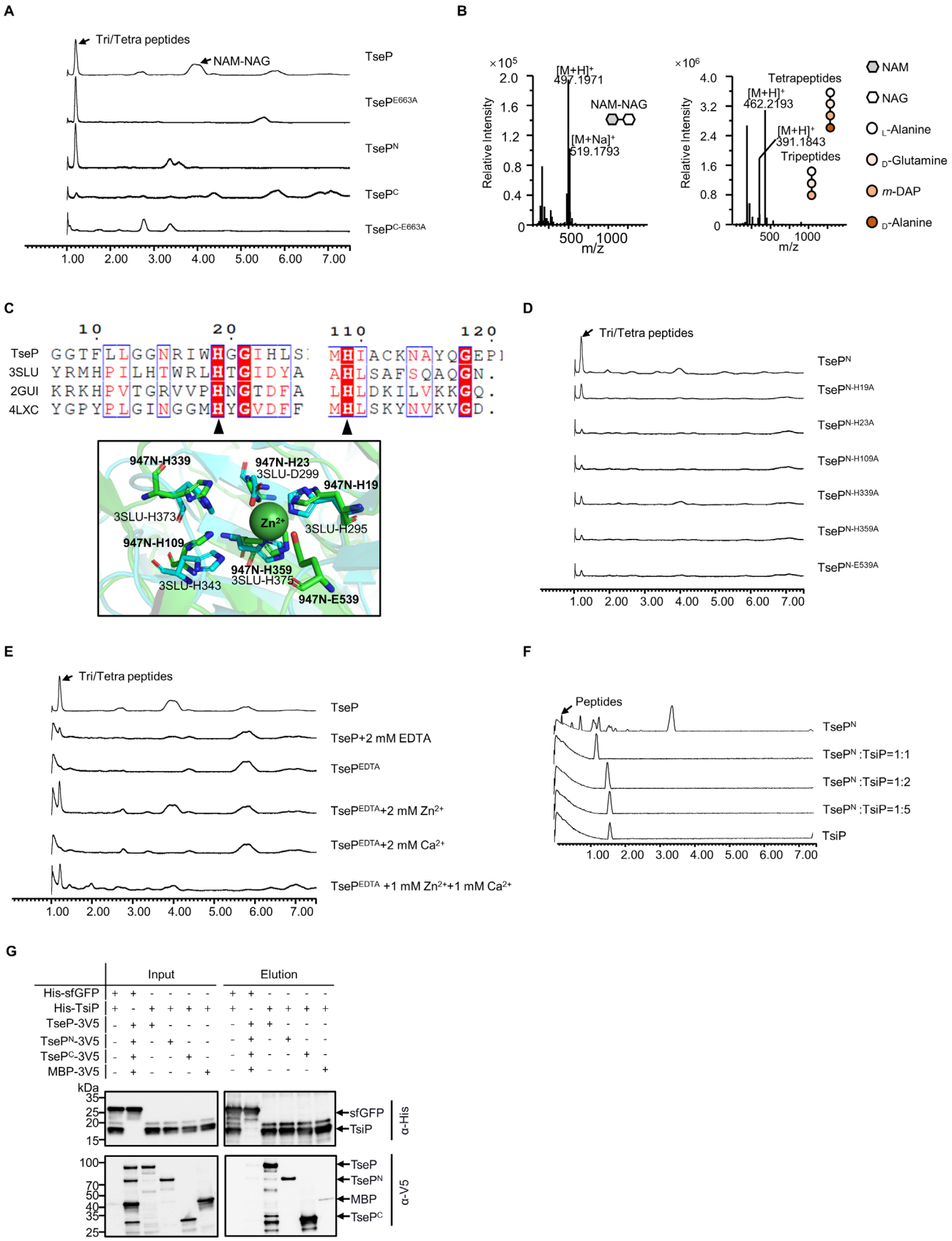
A
Tri/Tetra peptides
NAM-NAG
TseP
TseP^E663A
TseP^N
TseP^C
TseP^C-E663A
1.00 2.00 3.00 4.00 5.00 6.00 7.00
B
×10^5
[M+H]+ 497.1971
NAM-NAG
[M+Na]+ 519.1793
Relative Intensity
m/z
×10^6
Tetrapeptides
[M+H]+ 462.2193
[M+H]+ 391.1843
Tripeptides
NAM
NAG
L-Alanine
D-Glutamine
m-DAP
D-Alanine
C
TseP
3SLU
2GUI
4LXC
947N-H339
947N-H23
3SLU-D299
947N-H19
3SLU-H373
Zn2+
3SLU-H295
947N-H109
947N-H359
3SLU-H343
3SLU-H375
947N-E539
D
Tri/Tetra peptides
TseP^N
TseP^N-H19A
TseP^N-H23A
TseP^N-H109A
TseP^N-H339A
TseP^N-H359A
TseP^N-E539A
E
Tri/Tetra peptides
TseP
TseP+2 mM EDTA
TseP^EDTA
TseP^EDTA+2 mM Zn2+
TseP^EDTA+2 mM Ca2+
TseP^EDTA +1 mM Zn2++1 mM Ca2+
F
Peptides
TseP^N
TseP^N :TsiP=1:1
TseP^N :TsiP=1:2
TseP^N :TsiP=1:5
TsiP
G
Input
Elution
His-sfGFP
His-TsiP
TseP-3V5
TseP^N-3V5
TseP^C-3V5
MBP-3V5
kDa
sfGFP
TsiP
α-His
TseP
TseP^N
MBP
TseP^C
α-V5

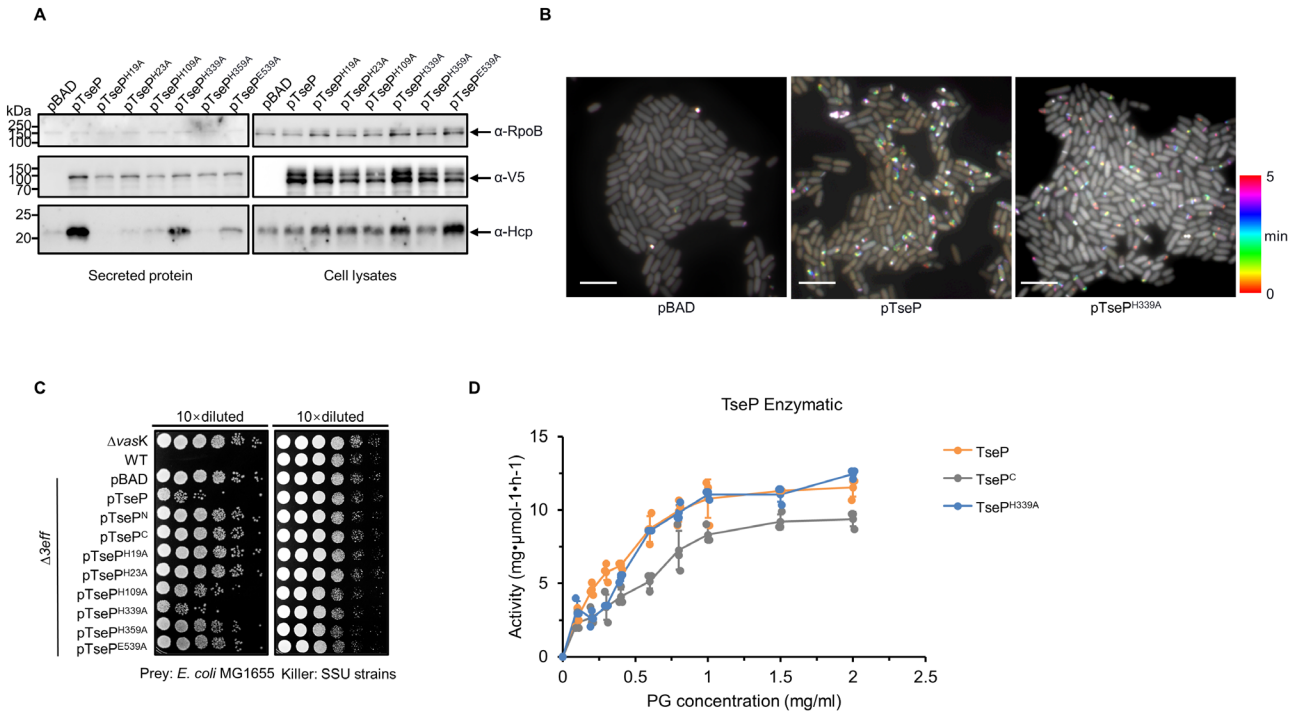
A
pBAD
pTseP
pTseP^H19A
pTseP^H23A
pTseP^H109A
pTseP^H339A
pTseP^H359A
pTseP^E539A
kDa
250
130
100
150
100
70
25
20
α-RpoB
α-V5
α-Hcp
Secreted protein
Cell lysates
B
pBAD
pTseP
pTseP^H339A
5
min
0
C
10×diluted
10×diluted
ΔvasK
WT
pBAD
pTseP
pTseP^N
pTseP^C
pTseP^H19A
pTseP^H23A
pTseP^H109A
pTseP^H339A
pTseP^H359A
pTseP^E539A
Δ3eff
Prey: E. coli MG1655 Killer: SSU strains
D
TseP Enzymatic
Activity (mg•μmol-1•h-1)
PG concentration (mg/ml)
0
5
10
15
0
0.5
1
1.5
2
2.5
TseP
TseP^C
TseP^H339A

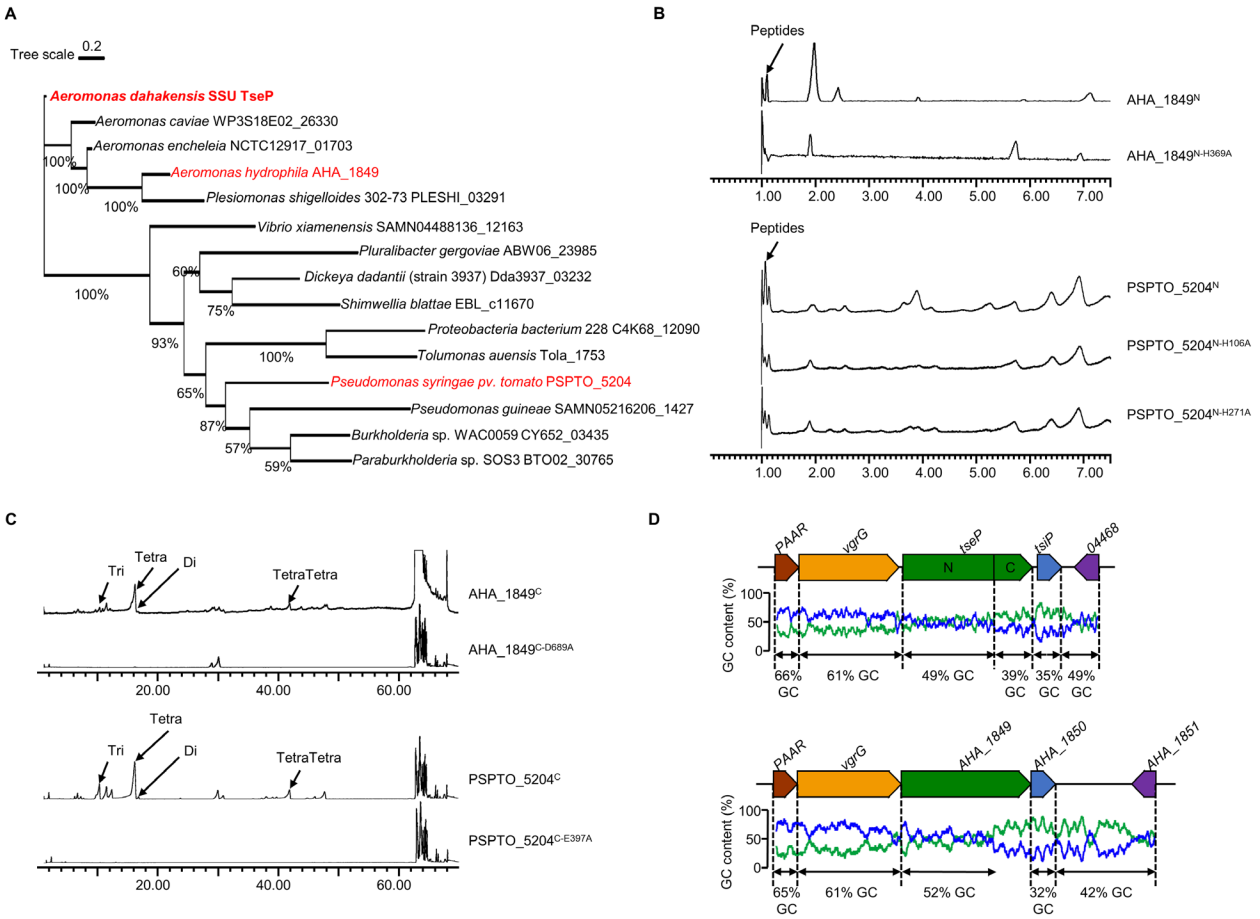

E

Homolog ID	E-Value	RMSD	Coverage (aa position)
Aeromonas schubertii WL1483_2262	4.62e-65	4.23	2-604
Fulvimonas soli C7456_107136	4.20e-24	1.3	606-844
Vibrio campbellii DSB67_24810	1.63e-19	1.88	639-840
Pseudomonas sp. HPB0071 N2J2S6	1.71e-21	1.57	611-844

F

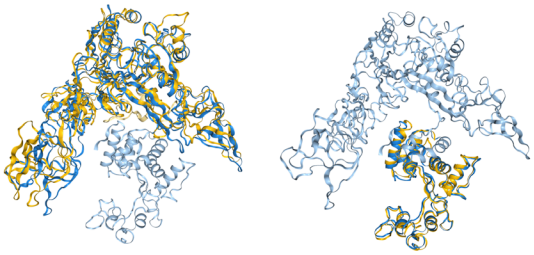

TseP vs WL1483_2262 TseP vs DSB67_24810

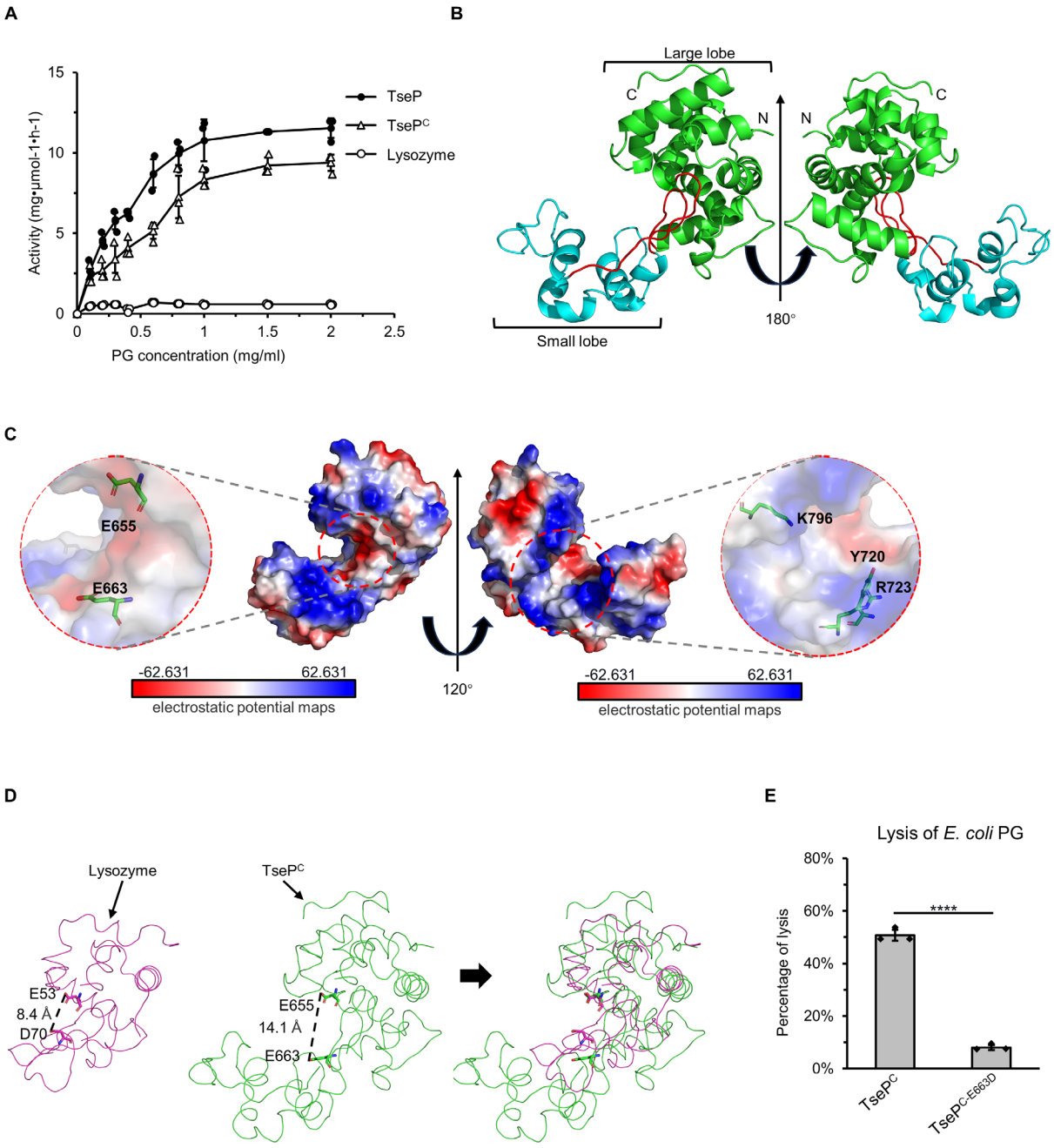
A
Activity (mg•µmol-1•h-1)
PG concentration (mg/ml)
TseP
TseP^C
Lysozyme
B
Large lobe
Small lobe
C
N
180°
C
E655
E663
K796
Y720
R723
-62.631
62.631
electrostatic potential maps
120°
D
Lysozyme
TseP^C
E53
8.4 Å
D70
E655
14.1 Å
E663
E
Lysis of E. coli PG
Percentage of lysis
****
TseP^C
TseP^C-E663D

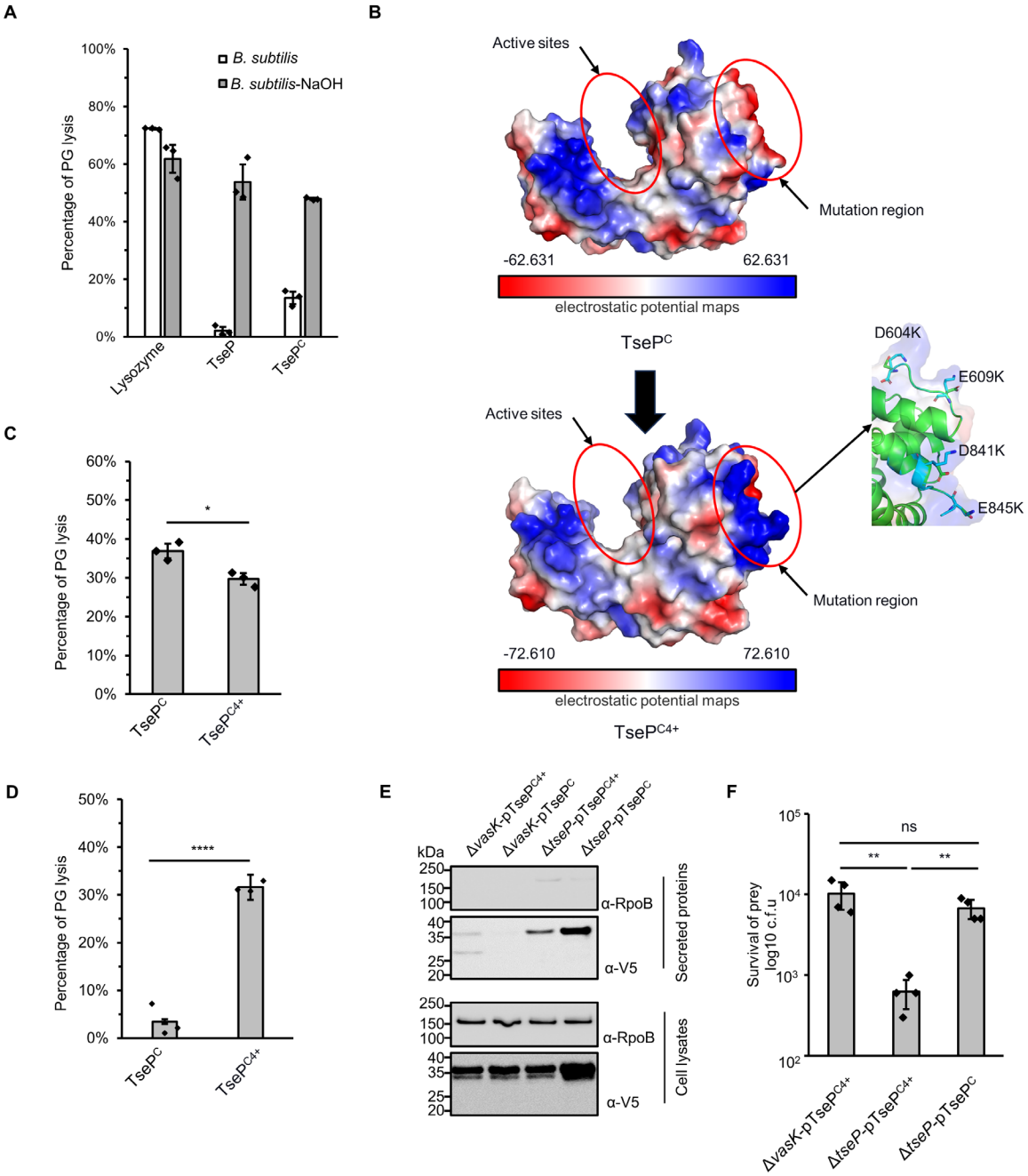
A
100%
80%
60%
40%
20%
0%
Percentage of PG lysis
B. subtilis
B. subtilis-NaOH
Lysozyme
TseP
TsePC
B
Active sites
Mutation region
-62.631
62.631
electrostatic potential maps
TsePC
D604K
E609K
D841K
E845K
Active sites
Mutation region
-72.610
72.610
electrostatic potential maps
TsePC4+
C
60%
50%
40%
30%
20%
10%
0%
Percentage of PG lysis
*
TsePC
TsePC4+
D
50%
40%
30%
20%
10%
0%
Percentage of PG lysis
****
TsePC
TsePC4+
E
kDa
ΔvasK-pTsePC4+
ΔvasK-pTsePC
ΔtseP-pTsePC4+
ΔtseP-pTsePC
250
150
100
α-RpoB
40
35
25
20
α-V5
Secreted proteins
250
150
100
α-RpoB
40
35
25
20
α-V5
Cell lysates
F
10^5
10^4
10^3
10^2
Survival of prey
log10 c.f.u
ns
**
**
ΔvasK-pTsePC4+
ΔtseP-pTsePC4+
ΔtseP-pTsePC

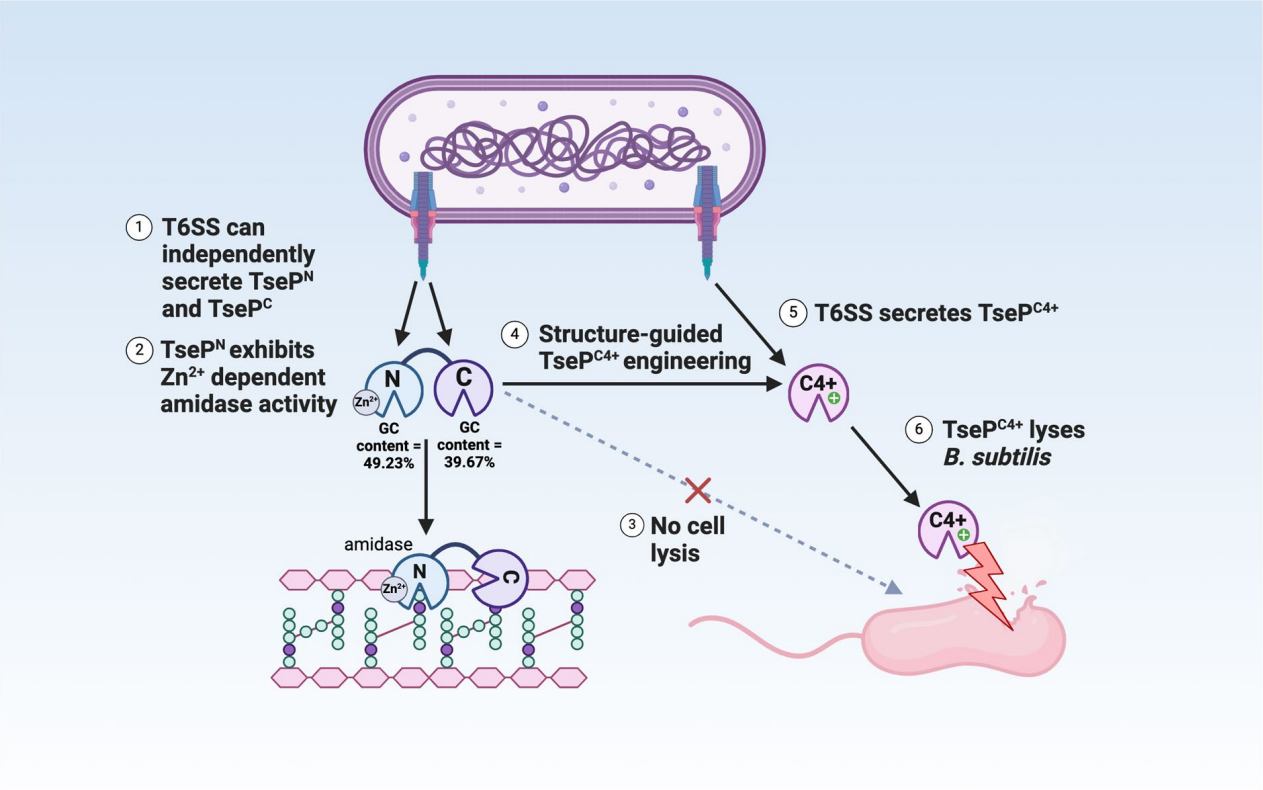
1 T6SS can independently secrete TseP^N and TseP^C
2 TseP^N exhibits Zn2+ dependent amidase activity
N
C
Zn2+
GC content = 49.23%
GC content = 39.67%
amidase
4 Structure-guided TseP^C4+ engineering
5 T6SS secretes TseP^C4+
C4+
6 TseP^C4+ lyses B. subtilis
3 No cell lysis

Table 1. Data collection and refinement statistics of $TseP^C$ crystallization

	$TseP^C$- 8XCL
Data collection	
Space group	*C 2 2 21*
a, b, c(Å)	44.48 138.80 95.83
α, β, γ(°)	90.00 90.00 90.00
Wavelength(Å)	0.97852
Resolution(Å)	47.91 – 2.27(2.40 – 2.27)
$CC_{1/2}$	0.984(0.840)
Unique reflections	25776 (4304)
R_{meas}(%)[a]	23.6(83.6)
Mean $I/\sigma(I)$[a]	6.1(2.6)
Completeness(%)[a]	95.9(99.4)
Multiplicity [a]	12.9(12.0)
Refinement	
Resolution(Å)	47.91 – 2.27
R_{work}/R_{free}[b]	0.189 / 0.227
No.atoms	
Protein	1910
Water	123
Average *B* factors (Å^2)	
Protein	31.72
Water	37.40
R.m.s. deviations	
Bond lengths(Å)	0.007
Bond angles(°)	0.871
Ramachandran plot	
Favored (%)	97.50
Allowed (%)	2.50
Outliers (%)	0.00

[a] The values in parentheses are for the outermost shell.
[b] R_{free} is the R_{work} based on 5% of the data excluded from the refinement.
$R_{meas} = \sum_{hkl}\sqrt{n/(n-1)}\sum_{i=1}^{n}|I_i(hkl) - \langle I(hkl)\rangle| / \sum_{hkl}\sum_i I_i(hkl)$, where $\langle I(hkl)\rangle$ is the mean intensity of a set of equivalent reflections.
$R_{work} = \sum_{hkl}||F_{obs}| - |F_{calc}|| / \sum_{hkl}|F_{obs}|$ where F_{obs} and F_{calc} are observed and calculated structure factors, respectively.

Supplemental Figure S1. TsiP inhibits both the amidase and lysozyme activities of TseP. The immunity protein TsiP was incubated with TseP or TseP^{C} on ice for 12 h before being mixed with PG. Products were analyzed by UPLC-QTOF-MS.

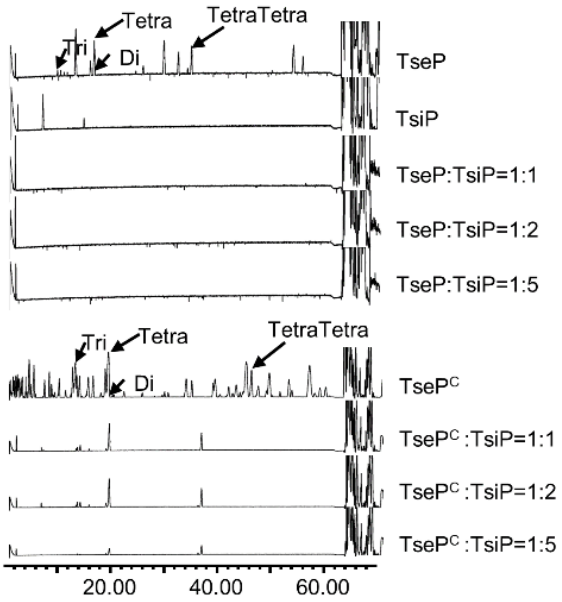

Supplemental Figure S2. The amidase activity of TseP is not required for either T6SS assembly or lysozyme function. A, Time-lapse imaging of VipA-sfGFP signals in the Δ*3eff* mutant complemented with different TseP amidase-inactive mutants. Each sample was captured every 10 s for 5 min and temporally color-coded. Color scale used to temporally color code the VipA-sfGFP signals is shown at the bottom. A 30 × 30 μm representative field of cells is shown. Scale bars, 5 μm. **B,** The maximum enzymatic activity of TseP and its variants. PG substrates (1.5 mg/ml) were treated with 10 nM TseP or its variants, respectively. Error bars indicate the mean ± standard deviation of three biological replicates, and statistical significance was calculated using a two-tailed Student's *t*-test. ns, not significant; *, $P < 0.05$; **, $P < 0.01$.

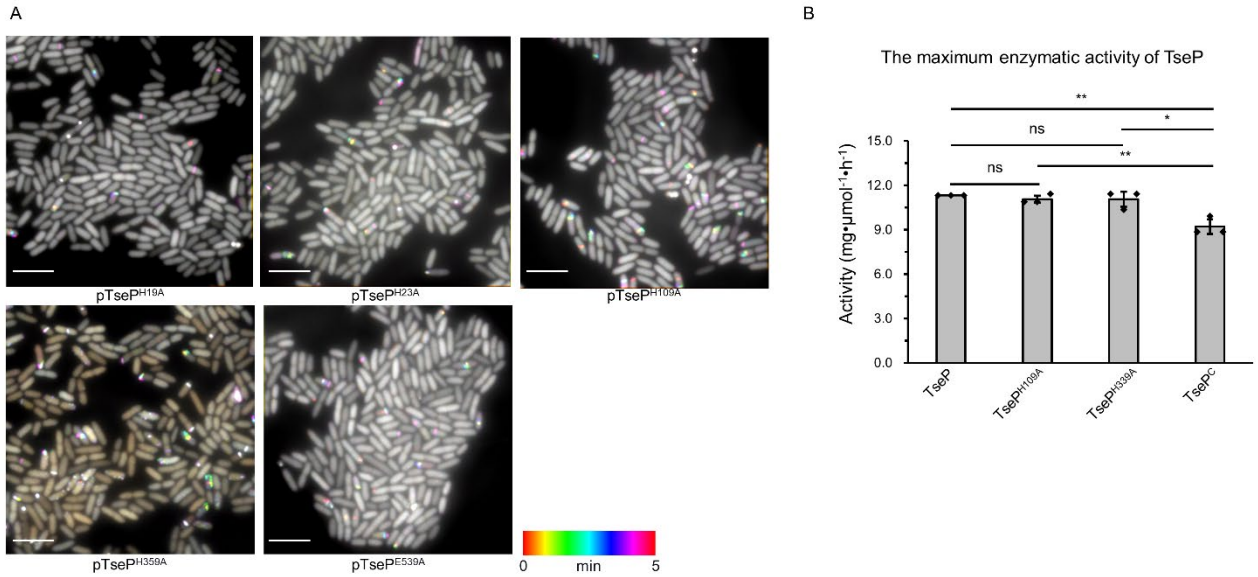

Supplemental Figure S3. Protein sequence analysis of the TseP homologs. Sequences were retrieved from UniProt and aligned using Jalview. Alignment view was generated using ESPript 3 with default settings. Proteins tested in this study are highlighted in red. The amidase active sites are marked with a black triangle at the bottom.

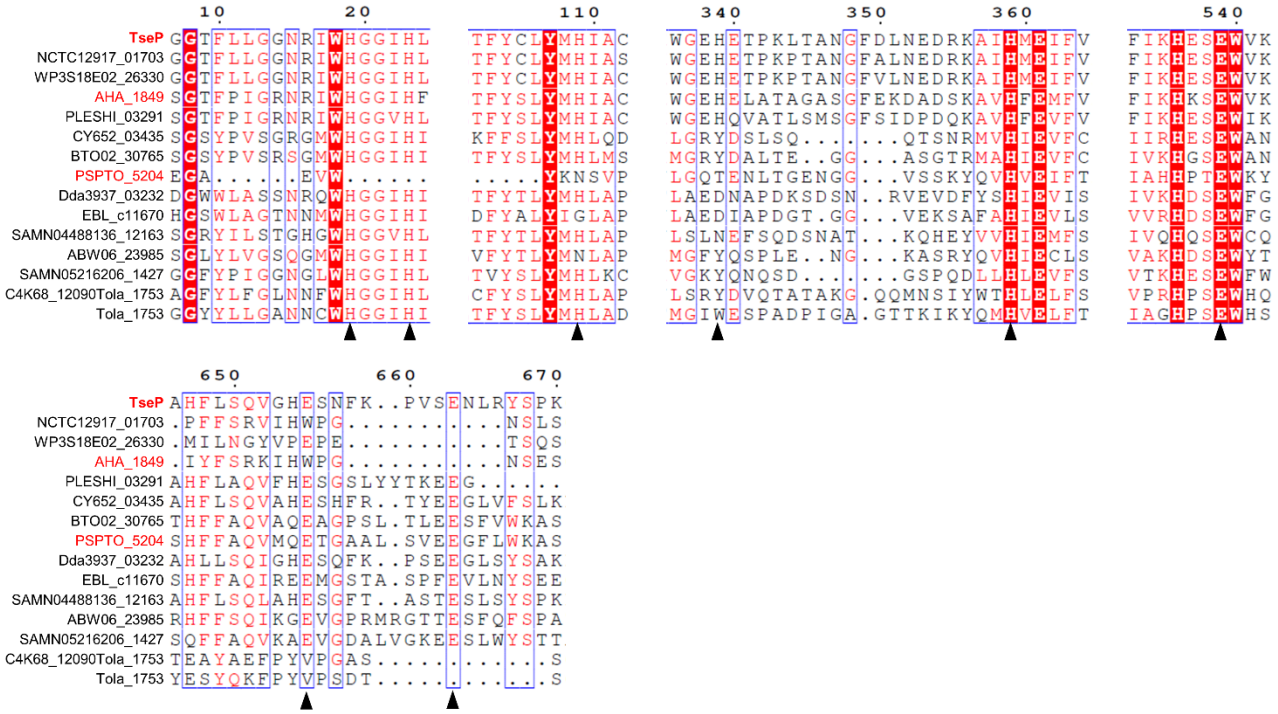

Supplemental Figure S4. Structural and mutational analyses of the C-terminal domain. A, Secondary structure analysis of $TseP^C$. Data was calculated using EMBL-EBI webs with PDBsum tool (https://www.ebi.ac.uk/thornton-srv/databases/pdbsum/). **B,** Electrostatic potential maps of the $TseP^C$ and lysozyme. The electrostatic surface potentials were colored red for negative charges, blue for positive charges, and white for neutral residues. **C,** Digestion of *B. subtilis* PG with different TseP variants. Exponential phase *B. subtilis* cells (OD_{600}~1.0) were used as substrates, and the lysis percentage was calculated by detecting the changes in optical density at 600 nm. **D,** Statistical analysis of killer cells during competition assays for which the survival of prey cells is shown in Figure 6F. For **C** and **D**, error bars indicate the mean ± standard deviation of three biological replicates, and statistical significance was calculated using a two-tailed Student's *t*-test. ns, not significant; **, $P < 0.01$.

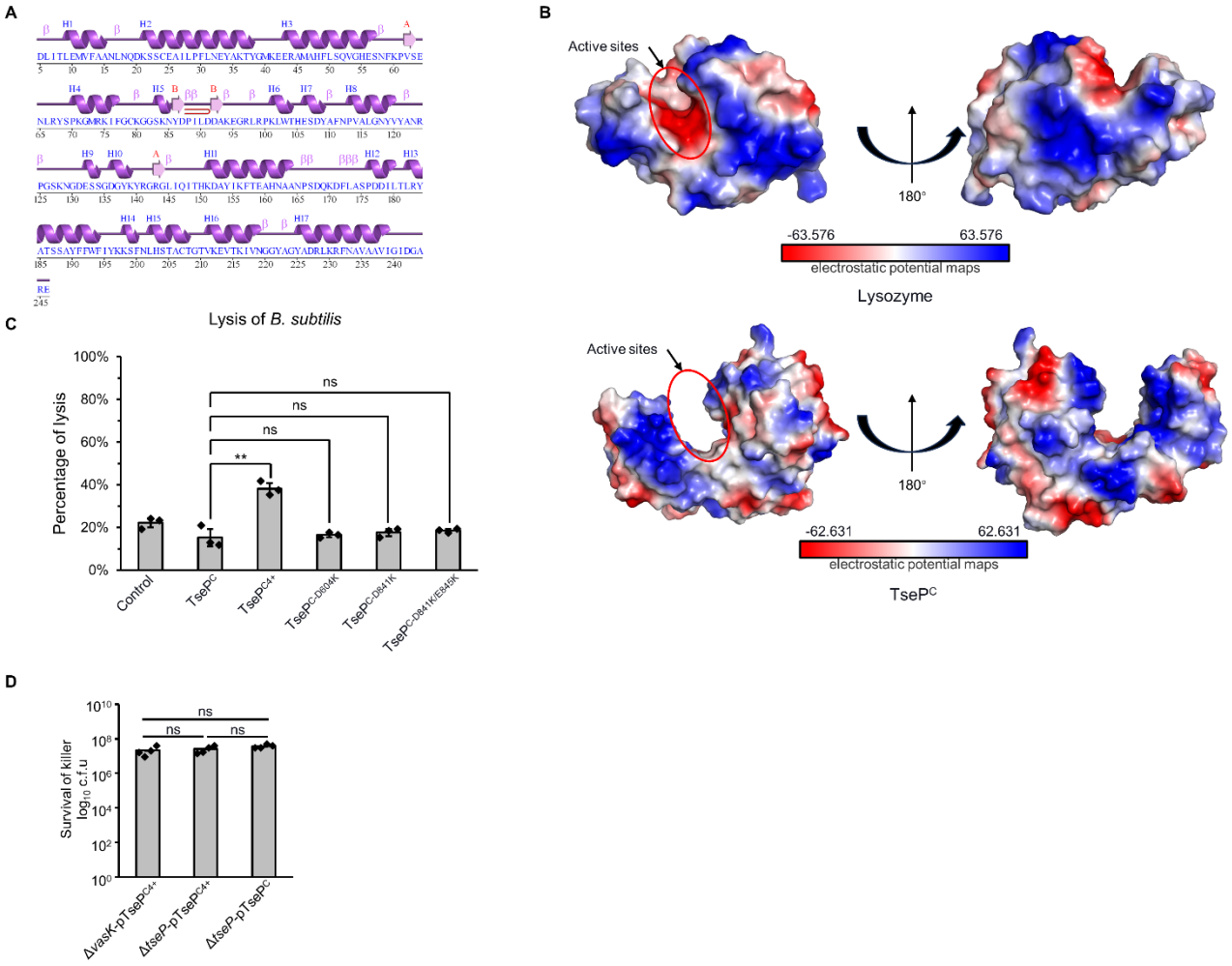
A
B
Active sites
180°
-63.576
63.576
electrostatic potential maps
Lysozyme
Active sites
180°
-62.631
62.631
electrostatic potential maps
TseP^C
C
Lysis of B. subtilis
Percentage of lysis
100%
80%
60%
40%
20%
0%
ns
ns
ns
**
Control
TseP^C
TseP^C4+
TseP^C-D694K
TseP^C-D841K
TseP^C-D841K/E845K
D
Survival of killer
log10 c.f.u
10^10
10^8
10^6
10^4
10^2
10^0
ns
ns
ns
ΔvasK-pTseP^C4+
ΔtseP-pTseP^C4+
ΔtseP-pTseP^C

Supplemental Figure S5. EF-hand domain has no effect on TseP activity. A, Protein sequence alignment (top) and structure alignment (bottom) of the EF-hand domain of TseP to the known EF-hand domain-containing protein $_{CD}$EFhd2 (PDB ID: 5H0P) (59). **B,** Statistical analysis of T6SS sheath assemblies in the Δ*3eff* mutant complemented with different TseP variants. Error bars indicate the mean ± standard deviation of three biological replicates, and statistical significance was calculated using a two-tailed Student's *t*-test. ns, not significant; **, $P < 0.01$. **C,** Competition assays of the Δ*3eff* mutant complemented with different TseP variants against *E. coli* MG1655. Competition assays were repeated twice.

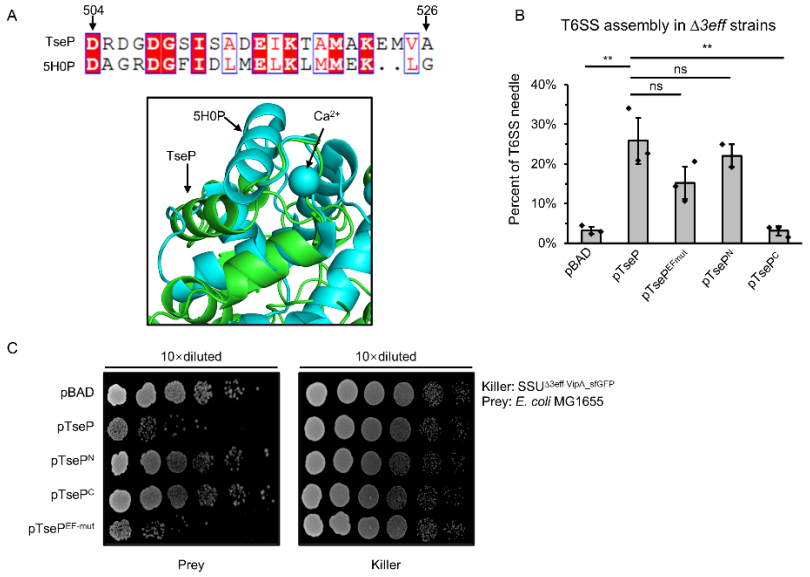

Supplemental Figure S6. Expression and secretion of TseP variants. A, Secretion analysis of Hcp in the Δ*3eff* mutant complemented with different TseP variants. RpoB serves as an equal loading and autolysis control. Hcp, RpoB, and 3V5-tagged TseP proteins were detected using specific antibodies. **B,** Protein expression of TseP and its variants in *E. coli* and SSU strains. RpoB serves as an equal loading control. RpoB and 3V5-tagged TseP proteins were detected using specific antibodies.

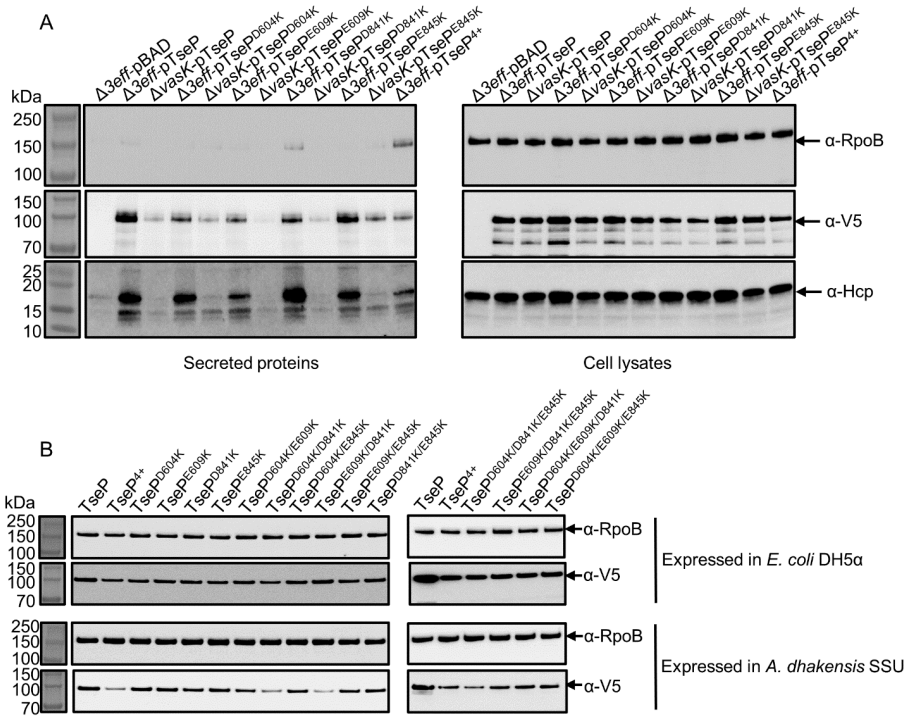

Supplemental Figure S7. Purification of TseP variants and homologous proteins. A, Purification of His-TseP, His-TseP^{E663A}, His-SUMO-TseP^{N}, His-SUMO-TseP^{C}, and His-SUMO-TseP$^{C\text{-}E663A}$. The His-SUMO tag was removed by SUMO protease. Proteins were used for PG-digestion analysis in Figure 2A, 2D, and 2E. **B,** Purification of TseP proteins with or without EDTA. Proteins were used for PG-digestion analysis in Figure 2E. **C,** Purification of TseP^{N} variants with a His-SUMO tag. The His-SUMO tag was removed by SUMO protease. Proteins were used for PG-digestion analysis in Figure 2D. **D,** Purification of AHA_1849, PSPTO_5204, and their mutants. Proteins were used for PG-digestion analysis in Figure 4B and 4C. **E,** Purification of TseP^{C} and TseP$^{C\text{-}E663D}$ with an His-SUMO tag. The His-SUMO tag was removed by SUMO protease. Proteins were used for PG-lysis in Figure 5E. **F,** Purification of TseP^{C} variants with an His-SUMO tag. The His-SUMO tag was removed by SUMO protease. Proteins were used for PG-lysis in Figure 6C and Figure S4C. All these proteins were purified with Ni-NTA affinity chromatography column, eluted using imidazole, and analyzed via SDS-PAGE.

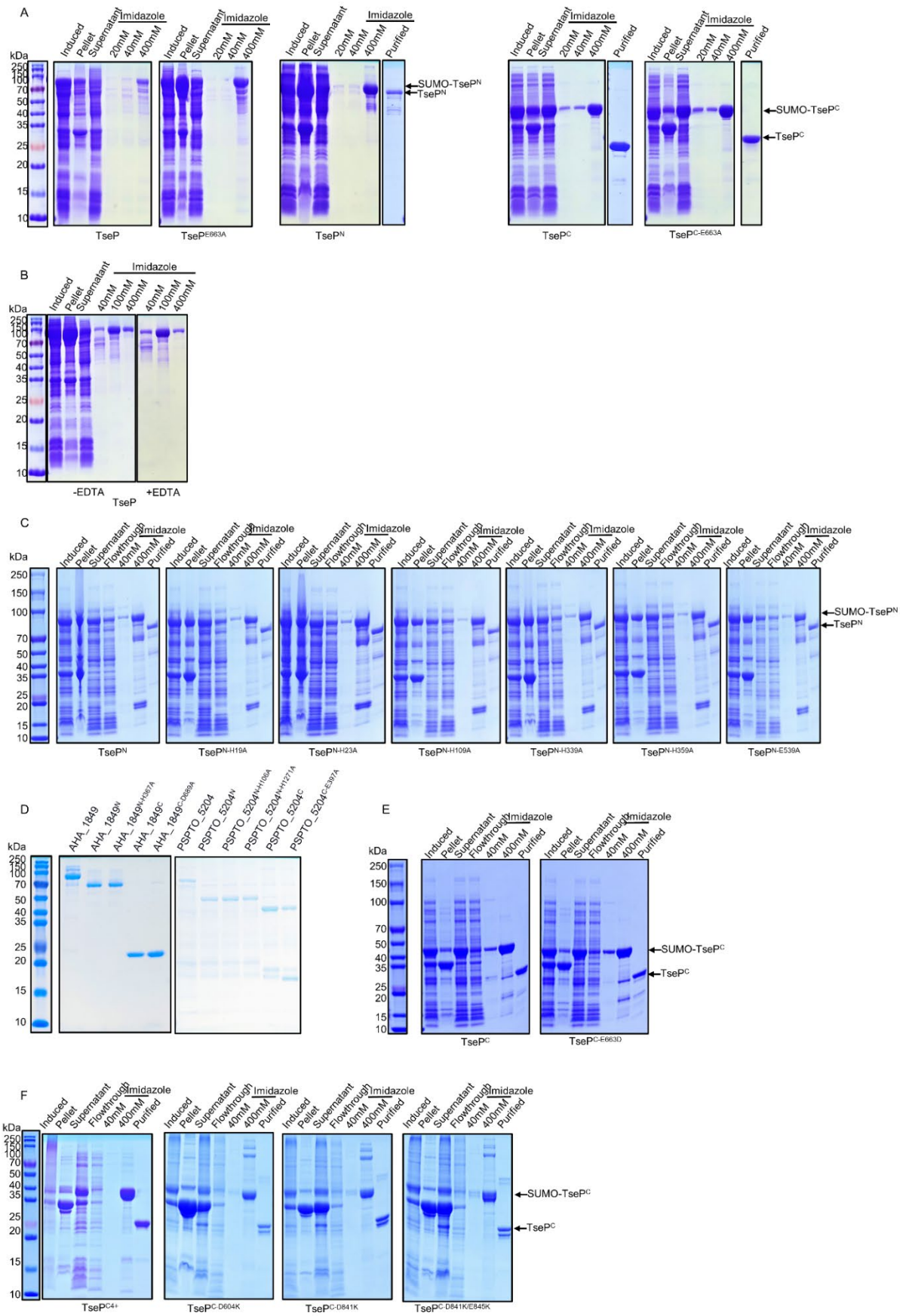
A
Induced
Pellet
Supernatant
Imidazole
20mM
40mM
400mM
Purified
kDa
250
150
100
70
50
40
35
25
20
15
10
SUMO-TseP^N
TseP^N
SUMO-TseP^C
TseP^C
TseP
TseP^E663A
TseP^N
TseP^C
TseP^C-E663A
B
100mM
-EDTA
+EDTA
C
Flowthrough
TseP^N
TseP^N-H19A
TseP^N-H23A
TseP^N-H109A
TseP^N-H339A
TseP^N-H359A
TseP^N-E539A
D
AHA_1849
AHA_1849^N
AHA_1849^N-H267A
AHA_1849^C
AHA_1849^C-D669A
PSPTO_5204
PSPTO_5204^N
PSPTO_5204^N-H196A
PSPTO_5204^N-H271A
PSPTO_5204^C
PSPTO_5204^C-E397A
E
TseP^C-E663D
F
TseP^C4+
TseP^C-D604K
TseP^C-D841K
TseP^C-D841K/E845K

Supplementary Table S1. Strains and plasmids used in this study.

Strain	Genotype	Description	Source
E. coli			
BL21(DE3)	*F– ompT gal dcm lon hsdSB(rB–mB–) λ(DE3 [lacI lacUV5T7p07 ind1 sam7 nin5]) [malB+]K-12(λS)*	Strain used for protein expression	Lab stock
DH5α	*F- Φ80lacZΔM15 Δ(lacZYA-argF) U169 recA1 endA1 hsdR17 phoA supE44 thi-1 gyrA96 relA1 λ-*	Strain used for cloning	Invitrogen
T-fast	*F' proA+ B+ lacIq ΔlacZM15 / fhuA2 Δ(lac-proAB) glnV galK16 galE15 R(zgb-210::Tn10)TetR endA1 thi-1 Δ(hsdS-mcrB)5*	Strain used for cloning	TIANGEN
MG1655	*F-, lambda-, rph-1*	K-12 wild-type strain used as prey for T6SS killing	Lab stock
Aeromonas dhakensis SSU	WT	Parental strain	[1]
	Δ*vasK*	T6SS null, in-frame deletion of *vasK*	[1]
	Δ*tseP*	In-frame deletion of *tseP*	[1]
	Δ*3eff, vipA-sfgfp*	In-frame deletion of *tseP*, *tseI*, and *tseC*, and fusion expression of sfGFP protein and VipA protein.	This study

Plasmid

	Plasmid	Description	Source
pBAD24	pBAD24Kan	Arabinose inducible expression plasmid, kanamycin resistance	Lab stock
	pBAD24kan-VgrG2-TseP-V5	Arabinose inducible expression of VgrG2 and TseP	This study
	pBAD24kan-VgrG2-$TseP^N$-V5	Arabinose inducible expression of VgrG2 and $TseP^N$	This study
	pBAD24kan-VgrG2-$TseP^C$-V5	Arabinose inducible expression of VgrG2 and $TseP^C$	This study

	pBAD24kan-VgrG2-TseP^{H19A}-V5	Arabinose inducible expression of VgrG2 and TseP ^{H19A}	This study
	pBAD24kan-VgrG2-TseP^{H23A}-V5	Arabinose inducible expression of VgrG2 and TseP^{H23A}	This study
	pBAD24kan-VgrG2-TseP^{H109A}-V5	Arabinose inducible expression of VgrG2 and TseP^{H109A}	This study
	pBAD24kan-VgrG2-TseP^{H339A}-V5	Arabinose inducible expression of VgrG2 and TseP^{H339A}	This study
	pBAD24kan-VgrG2-TseP^{H359A}-V5	Arabinose inducible expression of VgrG2 and TseP^{H359A}	This study
	pBAD24kan-VgrG2-TseP^{E539A}-V5	Arabinose inducible expression of VgrG2 and TseP^{E539A}	This study
	pBAD24kan-VgrG2-TseP^{EFhandmut}-V5	Arabinose inducible expression of VgrG2 and TseP^{EFhandmut}	This study
pBAD18	pBAD18Cm	Arabinose inducible expression plasmid, choloramphenicol resistance	Lab stock
pET28a		IPTG inducible expression plasmid, gentamycin resistant	Lab stock
	pET28a-His-SUMO-TseP	IPTG inducible expression of SUMO-TseP fusion with an N-terminal 6×His tag	Lab stock
	pET28a-His-SUMO-TseP^{E663A}	IPTG inducible expression of SUMO-TseP^{E663A} fusion with an N-terminal 6×His tag	[2]
	pET28a-His-SUMO-TseP^{N}	IPTG inducible expression of SUMO-TseP fusion with an N-terminal 6×His tag	This study
	pET28a-His-SUMO-TseP^{N-H19A}	IPTG inducible expression of SUMO-TseP^{N-H19A} fusion with an N-terminal 6×His tag	This study
	pET28a-His-SUMO-TseP^{N-H23A}	IPTG inducible expression of SUMO-TseP^{N-H23A} fusion with an N-terminal 6×His tag	This study
	pET28a-His-SUMO-TseP$^{N-H109A}$	IPTG inducible expression of SUMO-TseP$^{N-H109A}$ fusion with an N-terminal 6×His tag	This study
	pET28a-His-SUMO-TseP$^{N-H339A}$	IPTG inducible expression of SUMO-TseP$^{N-H339A}$ fusion with an N-terminal 6×His tag	This study
	pET28a-His-SUMO-TseP$^{N-H359A}$	IPTG inducible expression of SUMO-TseP$^{N-H359A}$ fusion with an N-terminal 6×His tag	This study
	pET28a-His-SUMO-TseP$^{N-E539A}$	IPTG inducible expression of SUMO-TseP$^{N-E539A}$ fusion with an N-terminal 6×His tag	This study
	pET28a-His-SUMO-TseP^{C}	IPTG inducible expression of SUMO-TseP^{C} fusion with an N-terminal 6×His tag	This study

pET28a-His-SUMO-TseP$^{C\text{-}E663D}$	IPTG inducible expression of SUMO-TseP$^{C\text{-}E663D}$ fusion with an N-terminal 6×His tag	This study
pET28a-His-SUMO-TseP^{C4+}	IPTG inducible expression of SUMO-TseP^{C4+} fusion with an N-terminal 6×His tag	This study
pET28a-His-SUMO-TseP$^{C\text{-}D604K}$	IPTG inducible expression of SUMO-TseP$^{C\text{-}D604K}$ fusion with an N-terminal 6×His tag	This study
pET28a-His-SUMO-TseP$^{C\text{-}D841K}$	IPTG inducible expression of SUMO-TseP$^{C\text{-}D841K}$ fusion with an N-terminal 6×His tag	This study
pET28a-His-SUMO-TseP$^{C\text{-}D841K/E845K}$	IPTG inducible expression of SUMO-TseP$^{C\text{-}D841K/E845K}$ fusion with an N-terminal 6×His tag	This study
pET28a-His-SUMO-TsiP	IPTG inducible expression of SUMO-TsiP fusion with an N-terminal 6×His tag	This study
pET28a-His-SUMO-VgrG2	IPTG inducible expression of SUMO-VgrG2 fusion with an N-terminal 6×His tag	This study
pET28a-His-SUMO-AHA_1849	IPTG inducible expression of SUMO-AHA_1849 fusion with an N-terminal 6×His tag	This study
pET28a-His-SUMO-AHA_1849^{N}	IPTG inducible expression of SUMO-AHA_1849^{N} fusion with an N-terminal 6×His tag	This study
pET28a-His-SUMO-AHA_1849$^{N\text{-}H369A}$	IPTG inducible expression of SUMO- AHA_1849$^{N\text{-}H369A}$ fusion with an N-terminal 6×His tag	This study
pET28a-His-SUMO-AHA_1849^{C}	IPTG inducible expression of SUMO-AHA_1849^{C} fusion with an N-terminal 6×His tag	This study
pET28a-His-SUMO-AHA_1849$^{C\text{-}D689A}$	IPTG inducible expression of SUMO-AHA_1849$^{C\text{-}D689A}$ fusion with an N-terminal 6×His tag	This study
pET28a-His-SUMO-PSPTO_5204	IPTG inducible expression of SUMO-PSPTO_5204 fusion with an N-terminal 6×His tag	This study
pET28a-His-SUMO-PSPTO_5204^{N}	IPTG inducible expression of SUMO-PSPTO_5204^{N} fusion with an N-terminal 6×His tag	This study
pET28a-His-SUMO-PSPTO_5204$^{N\text{-}H106A}$	IPTG inducible expression of SUMO-PSPTO_5204$^{N\text{-}H106A}$ fusion with an N-terminal 6×His tag	This study
pET28a-His-SUMO-PSPTO_5204$^{N\text{-}H271A}$	IPTG inducible expression of SUMO-PSPTO_5204$^{N\text{-}H271A}$ fusion with an N-terminal 6×His tag	This study
pET28a-His-SUMO-PSPTO_5204^{C}	IPTG inducible expression of SUMO-PSPTO_5204^{C} fusion with an N-terminal 6×His tag	This study
pET28a-His-SUMO-PSPTO_5204$^{C\text{-}E397A}$	IPTG inducible expression of SUMO-PSPTO_5204$^{C\text{-}E397A}$ fusion with an N-terminal 6×His tag	This study

Supplementary Table S2. The sequence identity of the N-terminal of TseP and homologs. Sequence identity was calculated using ClustalW web server. Colors are assigned from blue to red indicating low to high sequence similarity, respectively.

	1	2	3	4	5	6	7	8	9	10	11	12	13	14	15
TseP		41.8	88.2	88.7	47.1	12.4	14.3	12.1	13	12.1	13.3	12.6	12.3	12.5	16.7
NCTC12917_01703	41.8		42.9	41.1	60.6	14.9	13.7	13	14.7	13.9	13.3	10.9	10	14.4	17.4
WP3S18E02_26330	88.2	42.9		88.5	46.8	13	12.8	10.9	15.1	12	12.8	12.4	12	13.7	17
AHA_1849	88.7	41.1	88.5		47.4	12.5	11.6	12.6	13.3	11.7	13	13.1	15.7	13.1	17.1
PLESHI_03291	47.1	60.6	46.8	47.4		14.5	13.9	13.4	16.3	12.6	13.5	11.1	14.6	13.8	17.5
CY652_03435	12.4	14.9	13	12.5	14.5		15.6	12.8	13.5	42.1	13.2	17.4	13.5	12.2	14.9
BTO02_30765	14.3	13.7	12.8	11.6	13.9	15.6		14	13.7	13.3	18.4	13.3	13.1	34.9	12.8
PSPTO_5204	12.1	13	10.9	12.6	13.4	12.8	14		12.3	10.7	13.2	13.2	15.3	13.4	14.6
Dda3937_03232	13	14.7	15.1	13.3	16.3	13.5	13.7	12.3		13.3	17.2	14.2	14.4	17.4	18.1
EBL_c11670	12.1	13.9	12	11.7	12.6	42.1	13.3	10.7	13.3		13.7	12.3	10.7	11.6	12.8
SAMN04488136_12163	13.3	13.3	12.8	13	13.5	13.2	18.4	13.2	17.2	13.7		11.8	13.5	17.3	14.9
ABW06_23985	12.6	10.9	12.4	13.1	11.1	17.4	13.3	13.2	14.2	12.3	11.8		11.6	12.4	12.2
SAMN05216206_1427	12.3	10	12	15.7	14.6	13.5	13.1	15.3	14.4	10.7	13.5	11.6		15.9	16.3
C4K68_12090Tola_1753	12.5	14.4	13.7	13.1	13.8	12.2	34.9	13.4	17.4	11.6	17.3	12.4	15.9		13.8
Tola_1753	16.7	17.4	17	17.1	17.5	14.9	12.8	14.6	18.1	12.8	14.9	12.2	16.3	13.8	

Supplementary Table S3. The sequence identity of the C-terminal of TseP and homologs. Sequence identity was calculated using ClustalW web server. Colors are assigned from blue to red indicating low to high sequence similarity, respectively.

	1	2	3	4	5	6	7	8	9	10	11	12	13	14	15
TseP		10	11.8	12.4	13.6	48.1	48.9	49.8	20.7	24.2	19.8	17.4	10.1	19.3	12.1
NCTC12917_01703	10		69.2	18.7	11.4	9.5	11.4	11.4	11.8	9.5	11.4	11.4	14.7	12.3	17.1
WP3S18E02_26330	11.8	69.2		17.1	11.3	12.2	10.9	11.8	11.3	10.9	11.8	10	14.9	11.8	15.4
AHA_1849	12.4	18.7	17.1		12.4	10.9	10.4	14	11.4	11.4	10.9	12.4	15	12.4	13.5
PLESHI_03291	13.6	11.4	11.3	12.4		14.2	14	14.1	13.9	13.1	13.2	13	13.6	14.6	11.6
CY652_03435	48.1	9.5	12.2	10.9	14.2		46.4	49.8	21	23.6	19.8	20.6	11.4	21.5	11.6
BTO02_30765	48.9	11.4	10.9	10.4	14	46.4		50.6	21.3	22.6	20.7	20.4	10.1	22.7	9.8
PSPTO_5204	49.8	11.4	11.8	14	14.1	49.8	50.6		22.4	24.6	20.3	17	10.5	21	10.3
Dda3937_03232	20.7	11.8	11.3	11.4	13.9	21	21.3	22.4		58.5	26.4	21.3	10.1	33.9	9.4
EBL_c11670	24.2	9.5	10.9	11.4	13.1	23.6	22.6	24.6	58.5		25.1	23.3	10.1	35.2	8.5
SAMN04488136_12163	19.8	11.4	11.8	10.9	13.2	19.8	20.7	20.3	26.4	25.1		21.1	9.7	25.1	10.3
ABW06_23985	17.4	11.4	10	12.4	13	20.6	20.4	17	21.3	23.3	21.1		12.7	18.9	10.7
SAMN05216206_1427	10.1	14.7	14.9	15	13.6	11.4	10.1	10.5	10.1	10.1	9.7	12.7		11	50.4
C4K68_12090Tola_1753	19.3	12.3	11.8	12.4	14.6	21.5	22.7	21	33.9	35.2	25.1	18.9	11		11.6
Tola_1753	12.1	17.1	15.4	13.5	11.6	11.6	9.8	10.3	9.4	8.5	10.3	10.7	50.4	11.6	

References

[1] X. Liang, R. Moore, M. Wilton, M. J. Q. Wong, L. Lam, and T. G. Dong. Identification of divergent type VI secretion effectors using a conserved chaperone domain. Proc. Natl. Acad. Sci. U. S. A. 2015, 112(29):9106–9111.

[2] X. Liang, T.-T. Pei, Z.-H. Wang, W. Xiong, L.-L. Wu, P. Xu, S. Lin, and T. G. Dong. Characterization of lysozyme-like effector TseP reveals the dependence of type VI secretion system (T6SS) secretion on effectors in *Aeromonas dhakensis* strain SSU. Appl. Environ. Microbiol. 87(12):e00435-21.

[3] X. Liang, T.-T. Pei, H. Li, H.-Y. Zheng, H. Luo, Y. Cui, M.-X. Tang, Y.-J. Zhao, P. Xu, and T. Dong. VgrG-dependent effectors and chaperones modulate the assembly of the type VI secretion system. PLOS Pathog. 2021, 17(12):e1010116.